1 **Cell Diameter in *Bacillus subtilis* is Determined by the Opposing Actions of Two Distinct**
2 **Cell Wall Synthetic Systems**
3
4 Michael F. Dion[1,2,8], Mrinal Kapoor[1,2,8], Yingjie Sun[1,2,8], Sean Wilson[1,2] Joel Ryan[3,4], Antoine Vigouroux[5,6],
5 Sven van Teeffelen[5], Rudolf Oldenbourg[7], and Ethan C. Garner[1,2,4*]
6

7 [1] Department of Molecular and Cellular Biology, Harvard University, Cambridge, United States.
8 [2] Center for Systems Biology, Harvard University, Cambridge, United States.
9 [3] Department of Biology II, Ludwig-Maximilians-Universität München, Martinsried, Germany
10 [4] Physiology Course, Marine Biological Laboratory, Woods Hole, USA.
11 [5] Synthetic Biology Laboratory, Institut Pasteur, Paris, France.
12 [6] Microbial Morphogenesis and Growth Laboratory, Institut Pasteur, Paris, France.
13 [7] Marine Biological Laboratory, Bell Center, Woods Hole, United States
14 [8] These authors contributed equally to this work.
15
16 Corresponding Author: Ethan C. Garner
17 NW 445.20, Northwest Building, 52 Oxford Street, Cambridge, MA 02138
18 *E-mail: egarner@g.harvard.edu
19

20 **Abstract**

21 Rod shaped bacteria grow by adding material into their cell wall via the action of two spatially distinct enzymatic systems:

22 The Rod system moves around the cell circumference, while the class A penicillin-binding proteins (aPBPs) are

23 unorganized. To understand how the combined action of these two systems defines bacterial dimensions, we examined how

24 each system affects the growth and width of *Bacillus subtilis*, as well as the mechanical anisotropy and orientation of

25 material within their sacculi. We find that rod diameter is not determined by MreB, rather it depends on the balance between

26 the systems: The Rod system reduces diameter, while aPBPs increase it. RodA/PBP2A can both thin or widen cells,

27 depending on its levels relative to MreBCD. Increased Rod system activity correlates with an increased density of directional

28 MreB filaments, and a greater fraction of directionally moving PBP2A molecules. This increased circumferential synthesis

29 increases the amount of oriented material within the sacculi, increasing their mechanical anisotropy and reinforcing rod

30 shape. Together, these experiments explain how the combined action of the two main cell wall synthetic systems build rods

31 of different widths, a model that appears generalizable: *Escherichia coli* containing Rod system mutants show the same

32 relationship between the density of directionally moving MreB filaments and cell width.

33

34

1

Introduction

While the length of *Bacillus subtilis* rods increases as a function of their growth rate [1], their width remains constant across different growth conditions [2]. How bacteria define and maintain these rod shapes with such precision is not understood, but it must involve mechanisms controlling both the rate and location of glycan insertion into the peptidoglycan (PG) sacculus, the enveloping heteropolymer meshwork that holds cells in shape [3]. In order to understand how bacteria grow in defined shapes, we need to understand not only where these enzymes act, but how their activity affects the geometry and arrangement of material within the sacculus.

The PG for cell elongation is synthesized by two families of penicillin-binding proteins (PBPs). The class A penicillin-binding proteins (aPBPs) both polymerize and cross-link glycans. The class B penicillin-binding proteins (bPBPs) cross-link [4,5] the glycans polymerized by the glycosyltransferase RodA [6]. bPBPs and RodA are components of the "Rod complex", a group of proteins essential for rod shape **(Figure 1A).** In *B. subtilis*, this contains RodA, the class B transpeptidase PBP2A, MreC, MreD, RodZ, and filaments of MreB, an actin homolog [7,8]. MreB polymerizes together with other MreB homologs into short, highly curved filaments on the membrane [9,10]. To maximize their interaction with the membrane these curved filaments deform to the membrane, orienting along the direction of highest inward membrane curvature, pointing around the rod width [11]. Oriented by their association with MreB filaments, the Rod complex moves directionally around the cell circumference, driven by the PG synthetic activity of RodA/PBP2A [12-15]. This radial motion of independent filament-enzyme complexes are believed to insert PG strands around the rod width [16].

aPBPs also affect rod shape, as *B. subtilis* cells lacking them are thinner [17]. Single molecule and biochemical studies indicate aPBPs and the Rod system are both spatially and functionally distinct [6,14]: While Rod complexes move around the cell width, aPBPs have never been seen to move directionally. Rather, they diffuse within the membrane, occasionally pausing and remaining immobile for a few seconds [14]. Furthermore, the synthetic activity of either aPBPs or the Rod complex can be inhibited without affecting the activity or motions of the other [6,14]. Given that both synthetic systems are required for growth, but that Rod complex activity is spatially organized while aPBP activity is not **(Figure 1A)**, it is not clear how these two PG synthetic machineries work together to create a rod-shaped sacculus of a given width.

Current models of rod width have focused on MreB filaments, attributing the altered widths of *Escherichia coli* MreB mutants

63   to possible changes in MreB filament curvature, twist, angle, or localization to negative Gaussian curvature [18-24]. Not only do

64   these models lack the effects of aPBP mediated synthesis, they are: A) theoretical, as these proposed changes in filament

65   curvature or twist have not been structurally validated, or B) difficult to reconcile in *B. subtilis*, which has no detectable

66   negative Gaussian curvature [11] or skew in filament angle relative to the cell body [11-13,25].

67   Rather than focusing on MreB alone, we sought to develop a more thorough understanding of how the synthesis of both

68   organized and unorganized PG affects the width and growth of *B. subtilis*, as well as their effects on the organization and

69   mechanics of cell wall material. We find that aPBP and Rod complex-mediated PG synthesis have opposing effects on rod

70   width, and that cell diameter depends on their balance. The rate cells add surface area is largely unaffected by the level of

71   any one system, unless both become limiting. As MreBCD expression increases and rods thin, we observe a greater density

72   of directionally moving MreB filaments and a greater fraction of directionally moving enzymes. Increased Rod complex

73   activity creates a greater proportion of oriented material within the sacculus, causing the rod to stretch less across its width

74   and more along its length in response to internal turgor. Finally, we show that the different widths of *E. coli* Rod mutants

75   also show correlation between the density of directionally moving MreB filaments and cell width, giving a simple,

76   generalizable model that may explain the role of the Rod system in cell width.

Results

The Rod and aPBP systems have opposing effects on cell diameter

79   The width of rod-shaped bacteria has been attributed to properties encoded within MreB filaments [19,21,24,26]. We reasoned

80   that if width were defined by MreB, then the *mreBCD* genes from larger bacteria should produce cells with larger diameters.

81   To test this, we replaced the *B. subtilis mreBCD* operon with the *mreBCD* operon from *Bacillus megaterium*, a nearly 2-fold

82   wider bacterium. Surprisingly, these cells grew as rods only slightly wider than wild type (WT) *B. subtilis,* and by further

83   overexpressing *B. megaterium mreBCD* cells became even thinner (36 nm) **(Figure 1B, S1A),** suggesting that MreB

84   filaments themselves do not encode a specific rod width.

85

86   We next examined how width changed as we independently controlled the levels of the two main *B. subtilis* PG synthetic

87   systems. We created strains where expression of PBP1 (the major aPBP, encoded by *ponA*) was under IPTG control. As

88   PG synthesis by the Rod system depends upon MreB [14], we created strains where the native *B. subtilis mreBCD* operon

89   was under xylose control. We grew these strains at different induction levels, then measured their steady-state widths using

90   fluorescence microscopy. For a subset of inductions, we measured the relative protein abundance using proteomic mass

91   spectrometry, normalizing to the levels in WT cells grown in CH media (**Supplemental File 1**).

92

93   Varying *mreBCD* inductions revealed the Rod system has a thinning effect on rod shape. In the lowest inductions supporting

94   growth, rods were ~2-fold wider than WT, with some cells losing rod shape. As we increased *mreBCD* induction, cells

95   became thinner, reaching WT width when MreB abundance recapitulated WT levels **(Figure 1C, Figure S1B).** Inductions

96   above this point resulted in cells becoming 33 nm thinner than WT, and thinner still (58 nm) in *mreBCD* merodiploids. As

97   above, these results demonstrate MreB filaments do not *define* a given rod diameter, rather as previously hypothesized [11,27],

98   they indicate the Rod system *reduces* cell diameter.

99

100   Different *ponA* inductions revealed that aPBPs have a widening effect: With no IPTG, cells contained 0.25 the amount of

101   WT PBP1, and were ~23% thinner than WT, similar to ∆*ponA* strains [17] **(Figure 1D, Figure S1C).** As we increased *ponA*

102   induction cells became wider, reaching WT widths when PBP1 abundance recapitulated WT levels. Inductions above this

103   point caused cells to become increasingly wider, and by expressing *ponA* under stronger promoters or in merodiploids, we

104   could produce rods almost twice WT diameter.

105

106   These results demonstrate that the aPBPs and Rod system have opposing effects: The circumferentially moving Rod

107   complex reduces cell diameter, while the spatially unorganized aPBPs increase diameter. We hypothesized that a balanced

108   expression of each system could produce WT diameter rods. We combined the IPTG-inducible *ponA* and xylose-inducible

109   *mreBCD* alleles into one "dual-inducible" strain. We found six different pairs of xylose and IPTG concentrations that

110   produced rods of WT diameter **(Figure 1E, Figure S1D),** even though individually, each induction resulted in perturbed

111   diameters in the singly-inducible parental strains **(Figure 1C-D).** Relative quantitation of protein levels revealed that, in the

112   induction pairs at or beneath WT levels, these cells contained reduced, but relatively balanced amounts of PBP1 relative to

113   MreB. To determine this balance in native conditions, we measured the widths and protein levels of WT cells grown in

114   different media that result in different growth rates **(Figure 1F, Figure S1E).** Together, this data suggested width depends

115   on the balance between the aPBP and the Rod systems. By plotting the ratio of the [Fold change PBP1] / [Fold change

116   MreB] for all conditions in the data sets against their width **(Figure 1G),** we found that *B. subtilis* maintains its diameter

117   within ~5% of WT only when this ratio was within a range of 0.8 to 1.5; outside of this range, cell diameter diverged. WT

118   cells in different media showed PBP1/MreB ratios ranging from 0.9 to 1.5. Likewise, the induction pairs yielding WT widths

119   in the dual-inducible strain were within 0.8 to 1.0, only when their levels did not exceed WT. In contrast, the single-inducible

120   *ponA* or *mreBCD* strains were within 5% of WT width only when the ratio was within this range; outside of it, width rapidly

121   diverged. Together, these results indicate that, at the level of PG insertion, cell width is affected by the levels of the two

122   opposing synthetic systems that insert material into the sacculus **(Figure 1H).**

123

124   **RodA can function outside of the Rod system to widen cells, but only when PBP2A is also in excess.** Given that

125   RodA acts within the Rod complex with PBP2A (encoded by *pbpA*) to synthesize PG [14], titrations of *rodA* and *pbpA* should

126   show the same "thinning effect" as *mreBCD*. However, *rodA* overexpression can restore WT width to ΔaPBP cells [6], a

127   widening activity similar to *ponA.* To investigate this discrepancy, we made two sets of strains where *rodA* or *pbpA* (as the

128   only elongation-specific bPBP in the cell) were under the control of increasingly strong inducible promoters. As before [28,29],

129   low *rodA* or *pbpA* yielded wide cells; and as induction increased, cells gradually thinned to WT width, suggesting both are

130   required for functional Rod complexes. However, while we expected excess RodA to create thinner cells, once *rodA*

131   induction exceeded the level required for normal width, it behaved like excess *ponA*, fattening cells far beyond WT diameter

132   [6] **(Figure 2A).** In contrast, *pbpA* inductions beyond this point had a negligible effect on diameter.

133

134   Given that RodA and PBP2A must interact to synthesize PG [30], we tested if the widening caused by RodA overexpression

135   required excess PBP2A. We created two strains that had *rodA* under xylose control; one contained native *pbpA*, and the

136   other had *pbpA* under IPTG control (both as the only elongation-specific bPBP in the cell). As before, when *pbpA* was under

137   native control, depletion or overexpression of *rodA* caused diameter to increase **(Figure 2B).** In contrast, when *pbpA* was

138   held at the lowest induction required for WT width and *rodA* was simultaneously overexpressed, cells remained at WT

139   widths. However, these RodA-overproducing cells could be made increasingly wider by increasing *pbpA* induction **(Figure**

140   **2B)**, demonstrating excess RodA requires excess PBP2A to increase width.

141

142   These results suggested RodA/PBP2A widens cells when their levels exceed the rest of the Rod complex. If this hypothesis

143   is correct, wide cells caused by RodA/PBP2A overexpression should become thinner if MreBCD is increased, perhaps

144   recruiting the diffusive excess RodA/PBP2A into circumferentially-moving, "thinning" Rod complexes. Indeed, while strong

145   induction of *rodA* made wide cells, simultaneous overexpression of a second copy of *mreBCD* reduced cell diameter

5

146 **(Figure 2C)**, a narrowing far greater than what we observed when overexpressing *mreBCD* in otherwise WT strains **(Figure**

147 **1C)**. Thus, the aPBP-like widening activity of RodA/PBP2A likely occurs once they exceed some level of MreBCD, possibly

148 reflecting a saturation of binding sites within Rod complexes.

149

150

151 **Growth rates are maintained across a wide range of enzyme levels, unless both systems become limiting.**

152 We next examined how each PG synthetic system affected the rate of cell growth in our dual-induction strain using two

153 assays: 1) single-cell measurements of the rate of surface area addition [31] under agar pads and 2) population measures of

154 growth in a shaking plate reader. First, we examined the growth of the dual-inducible strain at the *mreBCD* and *ponA*

155 inductions that produced WT widths **(Figure 1E)**. At the lowest induction pairs, growth was greatly reduced in both assays,

156 and increased with each increasing induction pair **(Figure 2D)**, up to the induction pair that produced WT PBP1 and MreB

157 protein levels. Thus, growth can be reduced if both PG synthesis systems become limiting.

158

159 Next, we assayed growth as we titrated either *mreBCD* or *ponA* while holding the other constant. Similar to *E. coli* MreB

160 studies [22,32,33], both assays showed no difference in growth across a wide range of *mreBCD* inductions, except at the lowest

161 induction where cells frequently lost rod shape. Similarly, both assays saw no difference in growth across our *ponA*

162 induction range. Thus, even though these cells have different geometries, they add new surface area at the same rate. We

163 next examined how extremely low levels of aPBPs affected growth. Similar to previous observations [17,34,35], both Δ*ponA* and

164 ΔaPBP (Δ*pbpF, ΔpbpG, ΔpbpD, ΔponA*::*kan*) strains showed a marked reduction in bulk growth, a defect rescued by

165 overexpression of RodA [6,36]. However, the single cell measurements revealed a surprise: Both Δ*ponA* and ΔaPBP cells

166 showed no defect in their single-cell growth rate, adding surface area at the same rate as WT, as did RodA overexpressing

167 ΔaPBP cells **(Figure 2D)**. Given ΔaPBP cells display an increased rate of lysis that can be suppressed by RodA

168 overexpression [6,36], it appears the population growth rate defect of aPBP-deficient cells arises not from a reduction in growth

169 rate, but from an increased frequency of death.

170

171

172 **Increased MreBCD increases the density of directionally moving MreB filaments and the fraction of directionally**

173 **moving synthetic enzymes.**

6

174   To gain a mechanistic link between the level of the PG synthetic systems to cell width, we sought to develop microscopic

175   measures of their activity. While the fraction of stationary aPBPs would be difficult to quantify, Rod complexes exhibit a

176   more quantifiable phenotype: As their motion is driven by PG synthesis, the cellular activity of the Rod system can be

177   measured by quantitating the number of directionally moving MreB filaments [37]. We developed an analysis method that,

178   using total internal reflection fluorescence microscopy (TIRFM) data, determines the density of MreB filaments moving

179   directionally around the cell. Filaments undergoing directed motion are detected by taking advantage of the temporal

180   correlation occurring between adjacent pixels across the cell width as objects move through them. These objects are then

181   counted over a given time and then normalized to the total cellular surface area **(Figure 3A, S3A-F).** To evaluate the

182   robustness of this approach to filament number, velocity, angle, and length, we simulated TIRFM time-lapses of MreB

183   filaments in cells **(Figure S3G-K)**. This revealed this approach was more accurate than counting filaments in the same data

184   with particle tracking. Furthermore, when applied to real TIRFM movies of MreB filaments, this approach yielded numbers

185   comparable to tracking MreB filaments inside cells imaged with TIRF - structured illumination microscopy (TIRF-SIM)

186   **(Figure S3L)**. With this analysis tool, we examined how the density of directionally moving MreB filaments related to rod

187   width as we titrated the expression of an inducible *mreB-sw-msfGFP, mreCD* operon expressed as the only source at the

188   native locus. This analysis revealed a well fit, apparently linear correlation between directional filament density and width

189   (**Figure 3B**). Thus, the density of directionally moving MreB filaments reduces cell width, possibly by promoting directional

190   PG synthesis.

191

192   To this end, we next examined how MreBCD levels affected PBP2A motion. Multiple studies have noted PBP2A molecules

193   exist as a mixed population; some diffuse within the membrane, while others move directionally [12-14]. We titrated *mreBCD*

194   induction as we tracked the motions of PBP2A molecules (expressed at the native locus as a HaloTag fusion, sparsely

195   labeled with JF-549 [38]). At low *mreBCD*, only a small fraction of PBP2A moved directionally. As we increased *mreBCD*

196   induction, an increasing fraction of PBP2A molecules moved directionally **(Figure 3C, Movie SM1),** demonstrating that

197   *mreBCD* limits the amount of directional PBP2A.

198

199   **Increased MreBCD:PBP1 correlates with an increased amount of oriented material and structural anisotropy of the**

200   **cell wall.**

201   To gain more insight into how an increased density of directional rod complexes can reduce rod width, we used polarization

202   microscopy to understand how increased circumferential synthesis affected the organization of material within the cell wall.

203   Polarization microscopy reports on both the angle and extent of orientation within optically anisotropic (or birefringent)

204   materials [39], and has been used to assay the orientation of various materials, including plant cell walls [40-42] and mitotic

205   spindles [43]. Polarization microscopy revealed purified WT sacculi show birefringence, indicating that some fraction of the

206   material within them is oriented. Focused at their surface, sacculi showed a predominant slow axis oriented along the rod

207   length (**Figure 4A, Movie SM2**). Given that amino acids have a higher refractive index compared to sugars, this suggests

208   (in agreement with previous models [44]) the peptide crosslinks are predominantly oriented along the rod length, and the

209   glycans are oriented around the circumference.

210

211   We then examined how the balance between the Rod and aPBP systems affected the relative amount of oriented material

212   in the wall. We grew our dual-induction strain under three different induction conditions to create varied width cells: wide

213   (high *ponA*, low *mreBCD*), normal (*ponA* and *mreBCD* induced at WT levels), and skinny (low *ponA,* high *mreBCD*) (**Figure**

214   **4B**), purified their sacculi, and quantified their total retardance with polarization microscopy (**Figure 4C, Movie SM3**).

215   Retardance is the differential optical path length for light polarized parallel and perpendicular to the axis of molecular

216   alignment; alternatively, it is defined as birefringence (Δn) times the physical path length through an anisotropic material.

217   Wide cells (high *ponA*, low *mreBCD*) had the lowest retardance, skinny cells (low *ponA*, high *mreBCD*) had the highest

218   retardance, and normal cells were in between (**Figure 4D**). Because retardance depends on both the thickness of material

219   (path length) and the degree of its orientation (Δn), we normalized the retardance of each sample to the mean thickness of

220   the cell walls of each induction condition, obtained using transmission electron microscopy (**Figure S4A)**. This revealed that

221   the skinny cell walls had more highly ordered material (Δn) per path length (nm) of cell wall thickness, and that wide cell

222   walls had the least (**Figure 4E).** Thus, in agreement with recent atomic force microscopy studies showing orientated glycans

223   in *E. coli* require MreB [16], these experiments demonstrate that as Rod system activity increases, so does the amount of

224   oriented material in the wall.

225

226   The sacculi of *E. coli and B. subtilis* are mechanically anisotropic, stretching more along their length than across their width

227   [44-46]. To test how the ratio of oriented to unoriented PG synthesis affected this property, we grew our dual-inducer strain at

228   the three *mreBCD:ponA* inductions above, labeled their walls with Alexa-488-D-amino carboxamides [4], and assayed the

8

229   dimensions of their cell walls before and after hyperosmotic shocks (**Figure 4F-G**). This revealed that increased Rod system

230   activity correlated with an increased mechanical anisotropy of the sacculus: As we increased the expression of MreBCD

231   relative to PBP1A, rods shrank less across their width, and more along their length **(Figure 4H, S4B-C)**. Thus, the Rod

232   system acts to reinforce rod shape against internal turgor by promoting oriented PG synthesis around the rod.

233

234   ***E. coli* Rod mutants also show a correlation between cell width and the density of directionally moving filaments.**

235   Previous studies have examined how MreB and PBP2 mutations affect the shape of *E. coli*, hypothesizing that their

236   abnormal widths arise from changes in the curvature, twist, or angle of MreB filaments. Our observations in *B. subtilis*

237   suggested an alternative explanation: Abnormal width might arise from simply changing the amount of Rod system activity.

238   We tested this by measuring the density of directional GFP-MreB filaments in these same mutant *E. coli* strains. As a

239   benchmark, we first assayed the width of *E.coli* as we titrated the expression of mreB-sw-msfGFP using CRISPRi against

240   msfGFP [47] [28]. As in *B. subtilis,* this yielded an inverse relationship between directional MreB filament density and cell width

241   (**Figure 5A**). Examining each group of mutants showed the same result: 1) An identical trend was observed for the

242   mutations hypothesized to change filament twist [19], 2) as well as in the mutations designed to change filament curvature [24].

243   And 3) notably, the same correlation between directional filament density and cell width was observed in strains where *E.*

244   *coli mrdA* (PBP2) was replaced with *mrdA* genes from other species [22]. TIRF-SIM imaging of these MreB mutants revealed

245   some insight into these effects (**Movie SM4**): Some of the wide mutants showed either A) longer but fewer filaments, or B) a

246   large fraction of immobile filaments. Conversely, some thinner mutants appeared to have more, but shorter filaments. Finally

247   4), while Colavin et al. hypothesized that RodZ reduces width by changing MreB filament curvature [24], we found that

248   increased RodZ induction increased MreB filament density as cells thinned (**Figure 5B, Movie SM5**). This suggests that the

249   decrease in cell width most likely occurs from to RodZ's ability to nucleate MreB filaments [48] rather than changing their

250   curvature. Thus, the density of directionally moving Rod complexes correlates with cell width in both *B. subtilis* and *E. coli*

251   across multiple genetic perturbations.

252

253   **Discussion**

254   The shape of bacteria is defined by their cell walls; these experiments demonstrate that the two systems that insert PG into

255   it have opposing roles on its shape. Due to the intrinsic orienting of MreB filaments around the rod width [11], the Rod system

256   inserts circumferentially oriented material around the rod circumference, reducing its diameter. As the number of MreB

257 filaments increases, so does the fraction of directional enzymes and the amount of oriented material in the wall. In contrast,

258 the aPBPs do not move circumferentially, inserting material that isotropically enlarges the sacculus. Our data indicates the

259 macroscopic shape of the sacculus arises from the nature of the material inserted into it: The more it is oriented around the

260 rod circumference by the Rod complex, the less the rod stretches across its width, and the more it stretches along its length

261 **(Figure 5C)**.

262

263 If the balance between the two PG synthetic systems is perturbed, the shape of the sacculus becomes altered, though its

264 rate of expansion remains constant. As both systems utilize the same pool of lipid II [49], the flux through each may depend on

265 their relative levels; if one is reduced, the flux through the other may increase. This would explain why disrupting the Rod

266 system causes cells to swell [27,29,50-52]: In the absence of Rod-mediated thinning, aPBPs add more material uniformly over the

267 cell surface. Likewise, in the absence of aPBP-mediated widening, increased flux through the Rod system would explain

268 why cells become extremely thin [17,53]. However, if both systems are equivalently reduced, cells grow with normal widths, but

269 at slower rates; as long as the activities are balanced - identical shape arises from the balanced levels of enzymes, but

270 growth is reduced due to their combined activity becoming limiting. This would explain why *ponA* mutations rescue *mreB*

271 deletions [54]; equally crippling both systems may rebalance the activities such that the cell retains normal shape and viability.

272

273 **Implications for the role of MreB in rod width determination.**

274 Given that 1) *mreBCD* from the wide bacterium *B. megaterium* creates close to normal diameter *B. subtilis* rods, and 2) *B.*

275 *subtilis* diameter depends on *mreBCD* levels, we find it unlikely that any property of MreB filaments defines a given cell

276 diameter. Rather, MreB appears to be one component of a rod-thinning system, working in opposition to aPBP-mediated

277 widening. Indeed*, in vitro* studies have revealed MreB filaments are extremely curved (> 200 nm), allowing them to deform

278 to, and orient around the width of bacteria of any larger width [9,11]. While it remains possible that given MreB mutations or

279 interactions with RodZ could indeed alter filament curvature or twist [19,21,24,26], these experiments suggest a more

280 parsimonious explanation for their effect on Rod activity: These mutations alter MreB's polymerization dynamics or cellular

281 distribution. Reducing the amount or number of active MreB polymers would reduce Rod activity, causing cells to widen.

282 Likewise, mutations altering MreB's polymer length distribution or tendency for filaments to bundle would cause the

283 distribution of Rod activity to become non-uniform, causing some parts of the cell to thin while others would widen, as

284 previously observed for certain MreB mutants [12,27].

285

286 Additionally, our experiments reinforce observations that aPBPs and RodA (when in excess to MreBCD) serve reparative,

287 anti-lytic roles: aPBP-deficient cells grow at the same rate as WT, yet have an increased frequency of death, lysing as thin

288 rods without losing shape [6,36]. Likewise, aPBP-mediated synthesis increases upon endopeptidase overexpression in *E. coli*

289 [55]. Given the active state of aPBPs correlates with single aPBP molecules displaying periods of transient immobility [14,56],

290 their synthesis may be localized to small (<50 nm) regions. Combined, these observations support a model where aPBPs

291 synthesize material to fill gaps in the PG meshwork [36,14]. Gaps could arise via mechanical damage, hydrolases [55], or

292 between the imperfectly oriented strands built by the Rod complex [11]. If this model is correct, the different spatial activities of

293 these two systems might allow the sacculus to maintain integrity at any Rod/aPBP ratio: the fewer the Rod complexes, the

294 larger the gaps filled by aPBPs.

295

296 While many different activities affect the shape of the sacculus, such as its cleavage by hydrolases or rigidification by wall

297 teichoic acids [11], the first process defining its geometry is the spatial coordination controlling where glycans are inserted into

298 it. While these experiments give a coarse-grained description into how each synthetic system affects cell shape, a fine

299 scale, mechanistic understanding remains to be determined - How does aPBP activity make cells wider? How does

300 increased Rod activity make cells thinner? Understanding the physical mechanisms causing these changes will require not

301 only a better understanding of the molecular architecture of the sacculus, but also an investigation into how the enzymes

302 downstream of glycan insertion affect the shape and mechanics of sacculi as they subsequently modify, remodel, and break

303 down the nascently-polymerized glycan architecture.

304

305 **Acknowledgements**

313

Author Contributions.

B. subtilis strains were cloned by MD, YS, and MK. All width and bulk growth measurements of *B. subtilis* were done by MD,

and *E. coli* widths by YS. *E. coli* CRISPRi strains were cloned by AV, who was supervised by SVT. Single cell growth rates

were done by YS and MK. TIRFM and tracking of PBP2A was done by MK. All TIRFM of MreB was done by YS. TIRF-SIM

of MreB was done by YS, EG, and JR. Purified sacculi and proteomic mass spec sample preps were done by MD. YS wrote

the code for analysis of single cell growth rate, filament density, and simulations of data. Polarization microscopy and

analysis was conducted by JR, RO, and EG. SW did the FDAA synthesis, osmotic shocks, and TEM. The paper was written

by EG, MK, MD, and YS.

322

References

1. Vadia, S. & Levin, P. A. Growth rate and cell size: a re-examination of the growth law. *Curr Opin Microbiol* **24,** 96–103 (2015).
2. Sharpe, M. E., Hauser, P. M., Sharpe, R. G. & Errington, J. Bacillus subtilis cell cycle as studied by fluorescence microscopy: constancy of cell length at initiation of DNA replication and evidence for active nucleoid partitioning. *J Bacteriol* **180,** 547–555 (1998).
3. Vollmer, W., Blanot, D. & de Pedro, M. A. Peptidoglycan structure and architecture. *FEMS Microbiol Rev* **32,** 149–167 (2008).
4. Lebar, M. D. *et al.* Reconstitution of Peptidoglycan Cross-Linking Leads to Improved Fluorescent Probes of Cell Wall Synthesis. *J Am Chem Soc* **136,** 10874–10877 (2014).
5. Banzhaf, M. *et al.* Cooperativity of peptidoglycan synthases active in bacterial cell elongation. *Mol Microbiol* **85,** 179–194 (2012).
6. Meeske, A. J. *et al.* SEDS proteins are a widespread family of bacterial cell wall polymerases. *Nature* **537,** 634–638 (2016).
7. Jones, L. J., Carballido-López, R. & Errington, J. Control of cell shape in bacteria: helical, actin-like filaments in Bacillus subtilis. *Cell* **104,** 913–922 (2001).
8. van den Ent, F., Amos, L. & Löwe, J. Bacterial ancestry of actin and tubulin. *Curr Opin Microbiol* **4,** 634–638 (2001).
9. van den Ent, F., Izoré, T., Bharat, T. A., Johnson, C. M. & Lowe, J. Bacterial actin MreB forms antiparallel double filaments. *Elife* **3,** e02634 (2014).
10. Salje, J., van den Ent, F., de Boer, P. & Lowe, J. Direct membrane binding by bacterial actin MreB. *Mol Cell* **43,** 478–487 (2011).
11. Hussain, S. *et al.* MreB filaments align along greatest principal membrane curvature to orient cell wall synthesis. *Elife* **7,** 1239 (2018).
12. Garner, E. C. *et al.* Coupled, circumferential motions of the cell wall synthesis machinery and MreB filaments in B. subtilis. *Science* **333,** 222–225 (2011).
13. Domínguez-Escobar, J. *et al.* Processive Movement of MreB-Associated Cell Wall Biosynthetic Complexes in Bacteria. *Science* **333,** 225–228 (2011).
14. Cho, H. *et al.* Bacterial cell wall biogenesis is mediated by SEDS and PBP polymerase families functioning semi-autonomously. *Nat Microbiol* **1,** 16172 (2016).
15. van Teeffelen, S. *et al.* The bacterial actin MreB rotates, and rotation depends on cell-wall assembly. *Proc Natl Acad Sci USA* **108,** 15822–15827 (2011).
16. Turner, R. D., Mesnage, S., Hobbs, J. K. & Foster, S. J. Molecular imaging of glycan chains couples cell-wall polysaccharide architecture to bacterial cell morphology. *Nat Comms* **9,** 1263 (2018).
17. McPherson, D. C. & Popham, D. L. Peptidoglycan synthesis in the absence of class A penicillin-binding proteins in Bacillus subtilis. *J Bacteriol* **185,** 1423–1431 (2003).
18. Ursell, T. S. *et al.* Rod-like bacterial shape is maintained by feedback between cell curvature and cytoskeletal localization. *Proc Natl Acad Sci USA* **111,** E1025–34 (2014).

12

360   19.   Ouzounov, N. *et al.* MreB Orientation Correlates with Cell Diameter in Escherichia coli. *Biophys J* **111,** 1035–1043 (2016).

361   20.   Shi, H., Bratton, B. P., Gitai, Z. & Huang, K. C. How to Build a Bacterial Cell: MreB as the Foreman of E. coli Construction.
362   *Cell* **172,** 1294–1305 (2018).

363   21.   Wang, S. & Wingreen, N. S. Cell shape can mediate the spatial organization of the bacterial cytoskeleton. *Biophys J* **104,**
364   541–552 (2013).

365   22.   Tropini, C. *et al.* Principles of Bacterial Cell-Size Determination Revealed by Cell-Wall Synthesis Perturbations. *Cell*
366   *Reports* **9,** 1520–1527 (2014).

367   23.   Shi, H. *et al.* Deep Phenotypic Mapping of Bacterial Cytoskeletal Mutants Reveals Physiological Robustness to Cell Size.
368   *Curr Biol* **27,** 3419–3429.e4 (2017).

369   24.   Colavin, A., Shi, H. & Huang, K. C. RodZ modulates geometric localization of the bacterial actin MreB to regulate cell
370   shape. *Nat Comms* **9,** 1280 (2018).

371   25.   Olshausen, P. V. *et al.* Superresolution Imaging of Dynamic MreB Filaments in B. subtilis—A Multiple-Motor-Driven
372   Transport? *Biophys J* **105,** 1171–1181 (2013).

373   26.   Shi, H., Bratton, B. P., Gitai, Z. & Huang, K. C. How to Build a Bacterial Cell: MreB as the Foreman of E. coli Construction.
374   *Cell* **172,** 1294–1305 (2018).

375   27.   Harris, L. K., Dye, N. A. & Theriot, J. A. A Caulobacter MreB mutant with irregular cell shape exhibits compen... - PubMed -
376   NCBI. *Mol Microbiol* **94,** 988–1005 (2014).

377   28.   Vigouroux, A., Oldewurtel, E., Cui, L., Bikard, D. & van Teeffelen, S. Tuning dCas9's ability to block transcription enables
378   robust, noiseless knockdown of bacterial genes. *Molecular Systems Biology* **14,** e7899 (2018).

379   29.   Henriques, A. O., Glaser, P., Piggot, P. J. & Moran, C. P., Jr. Control of cell shape and elongation by the rodA gene in
380   Bacillus subtilis. *Mol Microbiol* **28,** 235–247 (1998).

381   30.   Fraipont, C. *et al.* The integral membrane FtsW protein and peptidoglycan synthase PBP3 form a subcomplex in
382   Escherichia coli. *Microbiology (Reading, Engl)* **157,** 251–259 (2010).

383   31.   Harris, L. K. & Theriot, J. A. Relative Rates of Surface and Volume Synthesis Set Bacterial Cell Size. *Cell* **165,** 1479–1492
384   (2016).

385   32.   Taheri-Araghi, S. *et al.* Cell-Size Control and Homeostasis in Bacteria. *Curr Biol* **27,** 1392 (2017).

386   33.   Zheng, H. *et al.* Interrogating the Escherichia coli cell cycle by cell dimension perturbations. *Proc Natl Acad Sci USA* **113,**
387   15000–15005 (2016).

388   34.   Murray, T., Popham, D. L. & Setlow, P. Bacillus subtilis cells lacking penicillin-binding protein 1 require increased levels of
389   divalent cations for growth. (1998).

390   35.   Popham, D. L. & Setlow, P. Phenotypes of Bacillus subtilis mutants lacking multiple class A high-molecular-weight
391   penicillin-binding proteins. *J Bacteriol* **178,** 2079–2085 (1996).

392   36.   Emami, K. *et al.* RodA as the missing glycosyltransferase in Bacillus subtilis and antibiotic discovery for the peptidoglycan
393   polymerase pathway. *Nat Microbiol* **2,** 16253 (2017).

394   37.   Billaudeau, C. *et al.* Contrasting mechanisms of growth in two model rod-shaped bacteria. *Nat Comms* **8,** 15370 (2017).

395   38.   Grimm, J. B. *et al.* A general method to improve fluorophores for live-cell and single-molecule microscopy. *Nat Meth* **12,**
396   244–250 (2015).

397   39.   Oldenbourg, R. Polarized light microscopy: principles and practice. *Cold Spring Harb Protoc* **2013,** (2013).

398   40.   Probine, M. C. & Preston, R. D. Cell Growth and the Structure and Mechanical Properties of the Wall in Internodal Cells of
399   Nitella opacaI. Wall structure and growth. *J Exp Bot* **12,** 261–282 (1961).

400   41.   Abraham, Y. & Elbaum, R. Quantification of microfibril angle in secondary cell walls at subcellular resolution by means of
401   polarized light microscopy. *New Phytol* **197,** 1012–1019 (2012).

402   42.   Baskin, T. I. Anisotropic expansion of the plant cell wall. *Annu Rev Cell Dev Biol* **21,** 203–222 (2005).

403   43.   Inouï ï, S. *Polarization Microscopy. Current protocols in cell biology* **1,** (John Wiley & Sons, Inc., 2001).

404   44.   Verwer, R. W., Beachey, E. H., Keck, W., Stoub, A. M. & Poldermans, J. E. Oriented fragmentation of Escherichia coli
405   sacculi by sonication. *J Bacteriol* **141,** 327–332 (1980).

406   45.   Gan, L., Chen, S. & Jensen, G. J. Molecular organization of Gram-negative peptidoglycan. *Proc Natl Acad Sci USA* **105,**
407   18953–18957 (2008).

408   46.   Yao, X., Jericho, M., Pink, D. & Beveridge, T. Thickness and elasticity of gram-negative murein sacculi measured by
409   atomic force microscopy. *J Bacteriol* (1999).

410   47.   Cui, L. *et al.* A CRISPRi screen in E. coli reveals sequence-specific toxicity of dCas9. *Nat Comms* **9,** 1912 (2018).

411   48.   Bratton, B. P., Shaevitz, J. W., Gitai, Z. & Morgenstein, R. M. MreB polymers and curvature localization are enhanced by
412   RodZ and predict E. coli's cylindrical uniformity. - PubMed - NCBI. *Nat Comms* **9,** 12510 (2018).

413   49.   Typas, A., Banzhaf, M., Gross, C. A. & Vollmer, W. From the regulation of peptidoglycan synthesis to bacterial growth and
414   morphology. *Nat Rev Microbiol* **10,** 123–136 (2011).

415   50.   Essential nature of the mreC determinant of Bacillus subtilis. *J Bacteriol* **185,** 4490–4498 (2003).

416   51.   Leaver, M. & Errington, J. Roles for MreC and MreD proteins in helical growth of the cylindrical cell wall in Bacillus subtilis.
417   *Mol Microbiol* **57,** 1196–1209 (2005).

418   52.   Fisher, I. C., Shapiro, L. & Theriot, J. A. Mutations in the nucleotide binding pocket of MreB can alter cell curvature and
419   polar morphology in Caulobacter. *Mol Microbiol* **81,** 368–394 (2011).
420   53.   Land, A. D. The requirement for pneumococcal MreC and MreD is relieved by inactivation of the gene encoding PBP1a. *J*
421   *Bacteriol* **193,** 4166–4179 (2011).
422   54.   Kawai, Y., Daniel, R. A. & Errington, J. Regulation of cell wall morphogenesis in Bacillus subtilis by recruitment of PBP1 to
423   the MreB helix. *Mol Microbiol* **71,** 1131–1144 (2009).
424   55.   Lai, G. C., Cho, H. & Bernhardt, T. G. The mecillinam resistome reveals a role for peptidoglycan endopeptidases in
425   stimulating cell wall synthesis in Escherichia coli. *PLoS Genet* **13,** e1006934 (2017).
426   56.   Lee, T. K., Meng, K., Shi, H. & Huang, K. C. Single-molecule imaging reveals modulation of cell wall synthesis dynamics in
427   live bacterial cells. *Nat Comms* **7,** 13170 (2016).
428

14

Figure 1 – Rod width depends on the relative levels of the widening aPBPs to the thinning Rod system.

Error bars are SD of the mean.

A. Schematic of the two PG synthetic systems responsible for growth. The *Rod complex* (depicted on the left) polymerizes glycans via the peptidoglycan glycosyltransferase (PGT) activity of RodA. These glycans are crosslinked into the sacculus by the transpeptidase (TP) activity of PBP2A. *aPBPs* are depicted on the right, containing both PGT and TP activity. *Below -* Schematic of each system's *in vivo* motions. Rod complexes move circumferentially around the rod as they synthesize PG. In contrast, aPBP synthesis does not appear organized, as they diffuse along the membrane, occasionally halting and remaining immobile for 1-3 seconds. Protein names are capitalized, gene names italicized.

B. *B. megaterium mreBCD* in *B. subtilis* forms rods close to *B. subtilis* width. "*B. sub*" indicates WT *B. subtilis*. "*B. meg*" indicates *B. megaterium*. Checkered boxes are bMD465 *(amyE::Pxyl-mreBCD, minCD [B. mega]::erm, mreBCD, minCD::spec [B. mega])*, a *B. subtilis* strain where the native *mreBCD* locus is replaced with *B. megaterium mreBCD*, and an additional *B. megaterium mreBCD* is under xylose control at an ectopic locus. "*B. meg mreBCD*" indicates bMD465 grown with 1% glucose to repress expression from the additional copy. "*2x B. meg mreBCD*" indicates bM465 growth with 30 mM xylose to overexpress *B. megaterium mreBCD* from the additional copy. See **Figure S1A** for a zoomed view.

C-F. Titrations of *ponA* and *mreBCD* vs. cell width. Each strain was grown in the inducer concentrations shown below the graph. Mean width is plotted on the left axis. PBP1 and MreB relative protein abundances (determined by mass spectrometry and normalized to the levels in WT Py79 grown in CH) are plotted on the right axis. Arrowhead indicates inductions producing WT widths and cellular levels of induced protein. Dashed line depicts mean steady state diameter of Py79 in CH, with SD shown as gray shaded area.

C. Cell diameter decreases with *mreBCD* induction. All data are from strain bMD545 (*amyE::Pxyl-mreBCD::erm ΔmreBCD::spec),* except for the induction marked * which are bMK355 (*amyE::Pxyl-mreBCD::erm*) containing a xylose-inducible *mreBCD* in addition to the native *mreBCD*. *Right* – Zoomed view of the right two bars compared to WT. P-value calculated with Mann-Whitney.
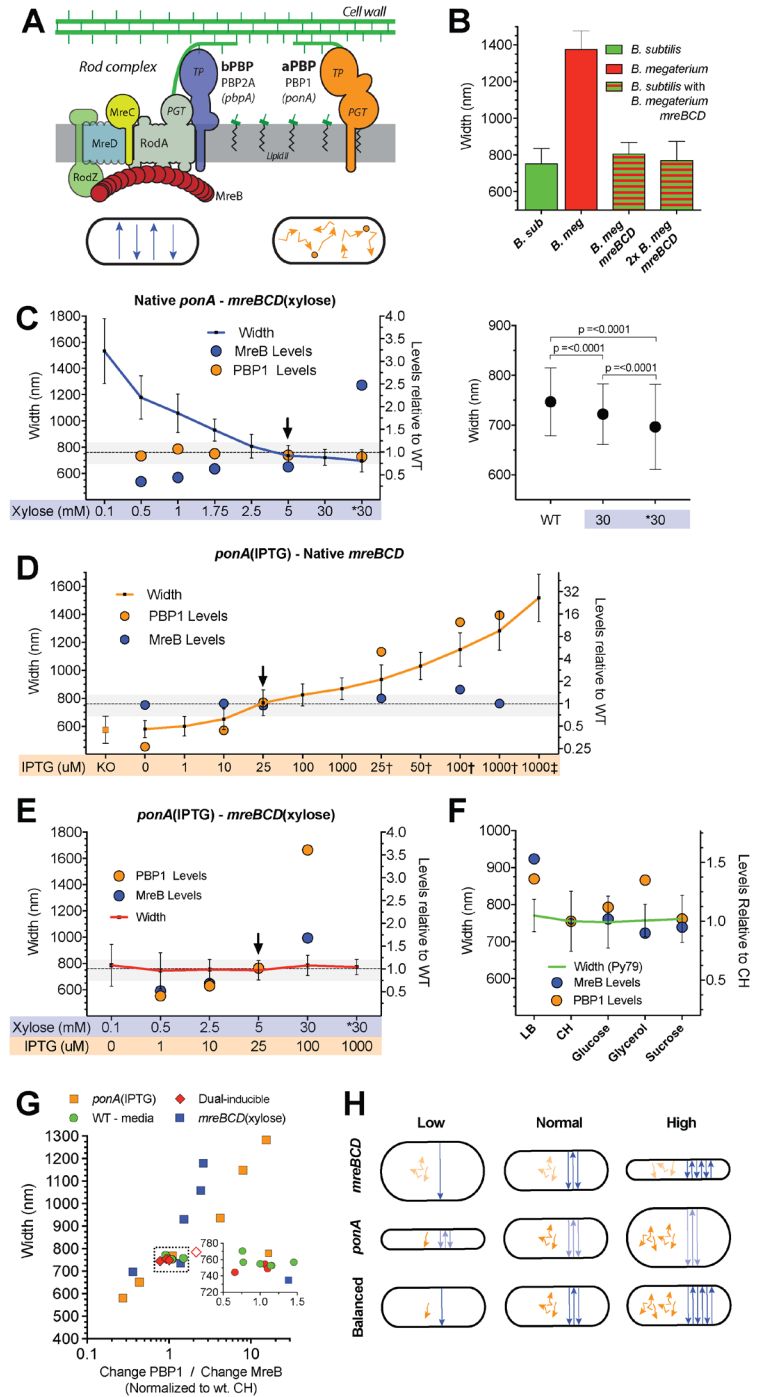
D. Cell diameter increases with *ponA* induction. All data are from strain bMD598 (*yhdG::Pspank-ponA*::*cat ΔponA::kan*), except for the inductions marked † and ‡ which are under stronger promoters than bMD598. † is bMD586 (*yhdG:Phyperspank-ponA*::*cat ΔponA::kan*), and ‡ is bMD554 (*yhdG::Phyperspank-ponA*::*cat*) which has an inducible *ponA* in addition to the native copy.

E. A balanced expression of both PG synthetic systems yields normal width rods across a large range.
Strain bMD620 (*amyE::Pxyl-mreBCD*::*erm ΔmreBCD::spec yhdH::Pspank-ponA*::*cat ΔponA::kan*) grown in combinations of inducers shown along the bottom. * indicates bMD622 (*amyE::Pxyl-mreBCD*::*erm yhdH::Pspank-ponA*::*cat ΔponA::kan*) containing a xylose-inducible *mreBCD* in addition to the native *mreBCD*.

F. *B. Subtilis* maintains a constant width in different media. Mean and SD of cell diameters of *B. subtilis* strain Py79 (exponential phase) grown in different growth media (media where a carbon source is indicated is S750). Width is plotted on the left axis. PBP1 and MreB relative protein abundances (determined by mass spectrometry, normalized to the levels in CH media) are plotted on the right axis.

G. WT width is maintained within a narrow range of relative PBP1/MreB ratios. Plotted are the widths of all cells in Figures 1C-F, against the ratio of the fold change in PBP1 to that of MreB. Inset is a zoomed view of the dotted box, showing the widths of cells within a 0.5-1.5 PBP1/MreB range. Green indicates ratios in different media. Orange squares indicate ratios in *ponA* inducible strains. Blue squares indicate ratios in *mreBCD* inducible strains. Red diamonds indicate ratios in the dual-induction strain, with the open red diamond indicating the ratio when protein levels exceeded WT.

H. Model for how the two PG synthesis systems affect rod width. *Top* – As the amount of circumferentially organized synthesis increases (blue straight lines), cell diameter decreases. *Center* – In contrast, as the level of unorganized synthesis increases (orange, non-directed lines), so too does cell diameter. *Bottom* – As long as the activities of the unorganized (orange) and circumferentially organized (blue) syntheses are balanced, cell width can remain constant, even across a range of protein levels.

Figure 2 – Effects of RodA/PBP2 on cell width, and how each PG synthetic system affects growth.

A. As *rodA* or *pbpA* induction is increased, the mean diameter of cells decreases up to a point, beyond which it increases with rising *rodA* induction, but not for *pbpA*. Green line represents diameters of bMD592 (Pxyl-*rodA*::*erm*) at five different xylose concentrations, save bMD580 (*yhdG*::Phyperspank-*rodA*::*cat ΔrodA::kan*) and bMD556 (*yhdG*::Phyperspank-*rodA*::*cat* - labeled †) which were induced with IPTG. Orange line represents the diameters of bMD597 (Pxyl-*pbpA*::*erm ΔpbpH::spec*) at five different xylose concentrations, save bMD574 (*yhdG*::Phyperspank-*pbpA*::*cat ΔpbpA::erm ΔpbpH::spec*) and bMD573 (*yhdG*::Phyperspank-*pbpA*::*cat ΔpbpH::spec* - labeled †) which were induced with IPTG.

B. Overexpression of *rodA* increases cell diameter, but only when *pbpA* expression is also sufficiently high. Light green bars represent the steady state diameter of bMD627 (Pxyl-*rodA*::*erm ΔpbpH::spec*) induced at the specified concentrations of xylose. Green + orange striped bars represent the steady state diameter of bMD631 (Pxyl-*rodA*::*erm yhdG*::Pspank-*pbpA::phleo ΔpbpH::spec*) induced at the specified concentrations of xylose and IPTG.

**C. The increase in cell diameter caused by overexpression of *rodA* is reduced by simultaneous overexpression of**

16
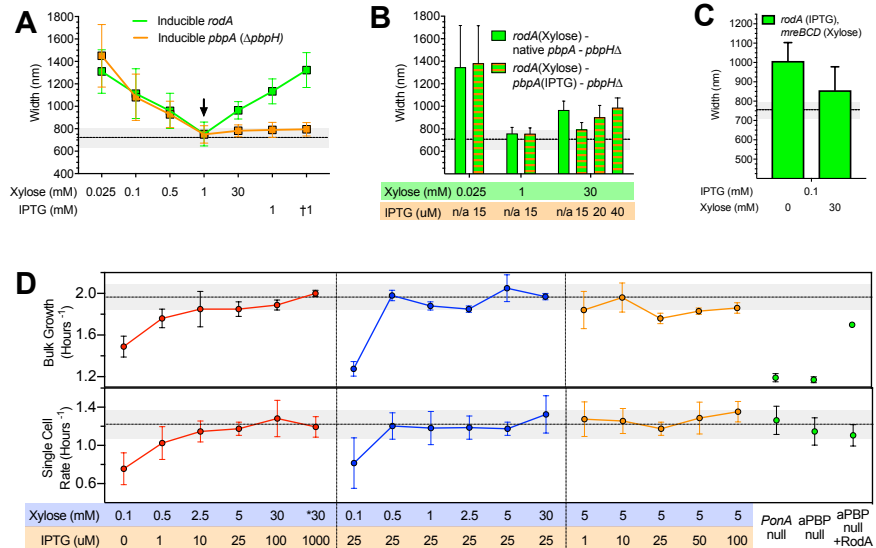
mreBCD. bMD557 (*yhdG*::Phyperspank-*rodA*::*cat amyE*::Pxyl-*mreBCD*::*erm)* was induced at the indicated levels of IPTG and xylose.

D. Rates of cell growth measured at the population (*Top*) and single cell (*Bottom*) level. Mean rates of cell growth were measured either by *(Top)* optical density at 600 nm in a shaking plate reader in CH, or (*Bottom*) by microscopically assaying the rate single cells (grown under an agar CH pad) added surface area. All measures are from bMD620 grown in the inducer concentrations indicated along the bottom, with the exception of: "*ponA* null", which is bMK005 (Δ*ponA*::*cat*), "aPBP null", which is bAM268 (Δ*pbpF,* Δ*pbpG,* Δ*pbpD,* Δ*ponA*::*kan*), and "aPBP Null + RodA", which is bAM288 (Δ*pbpF* Δ*pbpG* Δ*pbpD* Δ*ponA*:*kan amyE*::Phyperspank-*rodA-His10*::*spec*), where RodA is induced with 0.05 mM IPTG. Dotted horizontal lines represent the mean growth rate of Py79 in CH medium, with the shaded area representing the SD.

Figure 3 – Increased *mreBCD* increases directional MreB filament density and the fraction of directional PBP2A molecules.

A. Schematic of the method to quantitate directionally moving MreB filaments. Data shown is from simulated TIRFM time-lapses, with a 1 sec exposure time and 65 nm/pixel magnification. First, a kymograph is generated for each row of pixels along the midline of the cell. These kymographs are then lined up side by side to generate a single 2D image, where each column of the image contains a kymograph of each sequential row of pixels in the cell. This image is adaptively thresholded, then segmented with contour analysis to extract all fluorescent objects (middle). These objects are used to get velocity (slope), time (centroid), and position (row) for each particle. As each particle will show similar intensities in adjacent rows, or sometimes move at an angle, objects up to two rows apart are grouped based on time, position, and velocity. This yields the final particle count (bottom). See **Figure S3** for further details and tests.
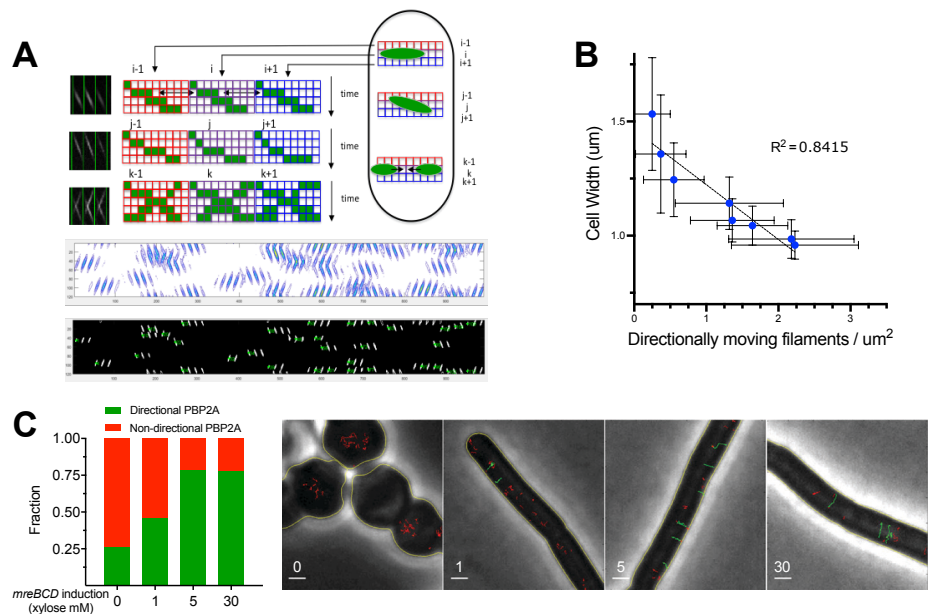
B. The decreased rod width caused by increasing *mreBCD* induction correlates with an increasing density of directionally moving MreB filaments. bYS981 (*amyE*::Pxyl-*mreB-SW-msfGFP, mreCD::erm ΔmreBCD::spec*) was grown in different amounts of xylose. Plotted are the steady state mean cell widths against the density of directionally moving filaments (determined as in **A**, above). All error bars are SD of the mean.

C. The fraction of directionally moving Halo-PBP2A molecules increases with *mreBCD* expression. *mreBCD* was induced at the indicated levels in bMK385 (*amyE*::Pxyl-*mreBCD*::*erm* Δ*mreBCD*::*spec HaloTag-11aa-pbpA*::*cat*), and the single molecule motions of JF-549-labeled Halo-PBP2A were imaged by TIRFM using 300 msec continuous exposures. Plotted are the fractions of labeled PBP2A trajectories over 7 frames in length that moved directionally. *Right* - Representative montage of Halo-PBP2A trajectories at different levels of *mreBCD* inductions overlaid on phase images. Directionally moving tracks are labeled green; all other tracks are labeled red. Scale bar is 1 μm. See also corresponding **Movie S3**.

589 **Figure 4 - Increased Rod activity increases both the amount of oriented material within**
590 **sacculi and their mechanical anisotropy.**

591
592 All error bars are SD of the mean.
593

594 **A. Polarization microscopy**
595 **reveals oriented material within**
596 **the cell wall.** *Left* - LC-PolScope
597 images of purified WT Py79 sacculi.
598 Focused at the surface, the cell wall
599 is seen to be birefringent. Color
600 indicates the orientation of the slow
601 axis, with intensity corresponding to
602 retardance in that direction.
603 Orientation key is the color wheel at
604 upper left. *Right* - Polarization
605 orientation view of the sacculi
606 surface, with lines pointing in the
607 predominant orientation of the slow
608 axis. See also **Movie S2.**
609

610 **B. Induction conditions used to**
611 **assay sacculi properties.** bMD620
612 (*amyE*::Pxyl-*mreBCD*::*erm*
613 Δ*mreBCD*::*spec yhdG*::Pspank-*ponA*::*cat*
614 Δ*ponA*::*kan*) was induced to grow at 3
615 different widths: Skinny (30 mM
616 xylose, 1 µM IPTG), Normal (5 mM
617 xylose, 25 µM IPTG), and Wide (0.5
618 mM xylose, 100 µM IPTG).
619

620 **C.** Example LC-PolScope image of
621 bMD620 sacculi induced at different
622 widths. For each experiment, pairs
623 of purified sacculi ("Wide" and
624 "Normal", or "Wide" and "Skinny")
625 were combined, and Z-stacks were
626 collected in 100 nm steps. See also **Movie S3.**
627

628 **D. The amount of oriented material in the cell wall increases with *mreBCD* induction, and inversely correlates with rod**
629 **width.** Plotted is the mean retardance vs. width along the length of projected Z-stacks of at least 90 different cells for each
630 induction condition.
631
632 **E.** Mean retardance for each sample normalized to the thickness of the cell wall, as measured by TEM.
633
634 **F. Schematic of osmotic shock assay of anisotropy.** *B. subtilis* sacculi are normally under tension due to the high internal turgor
635 (black arrows). Hyperosmotic shock negates this pressure, allowing observation of how sacculi shrink in length and width (colored
636 arrows).
637
638 **G.** Example FDAA-labeled cells from each condition (*left to right*: Skinny, Normal, Wide) before and after osmotic shock. Scale bar
639 is 1 µm.
640
641 **H. As the relative amount of Rod system activity increases, so does the mechanical anisotropy of the sacculus.** Anisotropy
642 (% change in length / % change in width) for each induction condition following osmotic shock. Raw data and reduction for each
643 dimension (both absolute and percent) are in **Figure S4.**

18
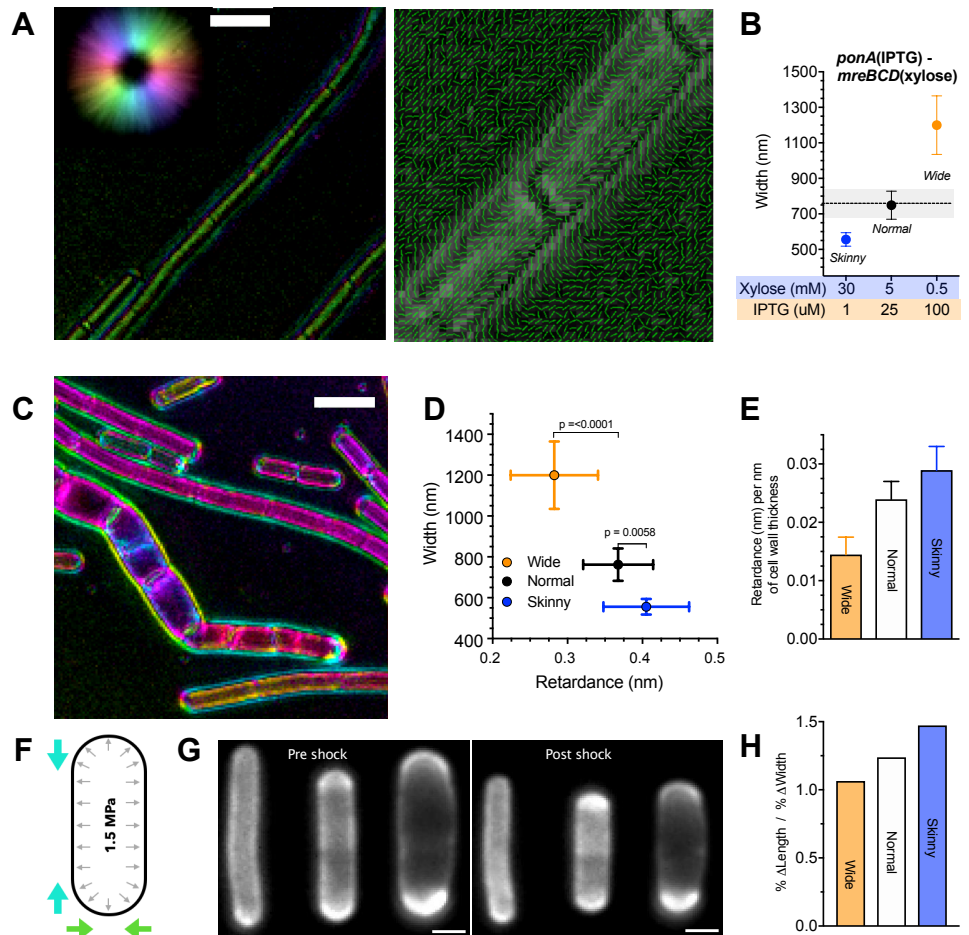
Figure 5 – Directional MreB filament density also correlates with cell width of *E. coli* Rod mutants, suggesting a generalizable model for the effects of Rod complex on cell width.
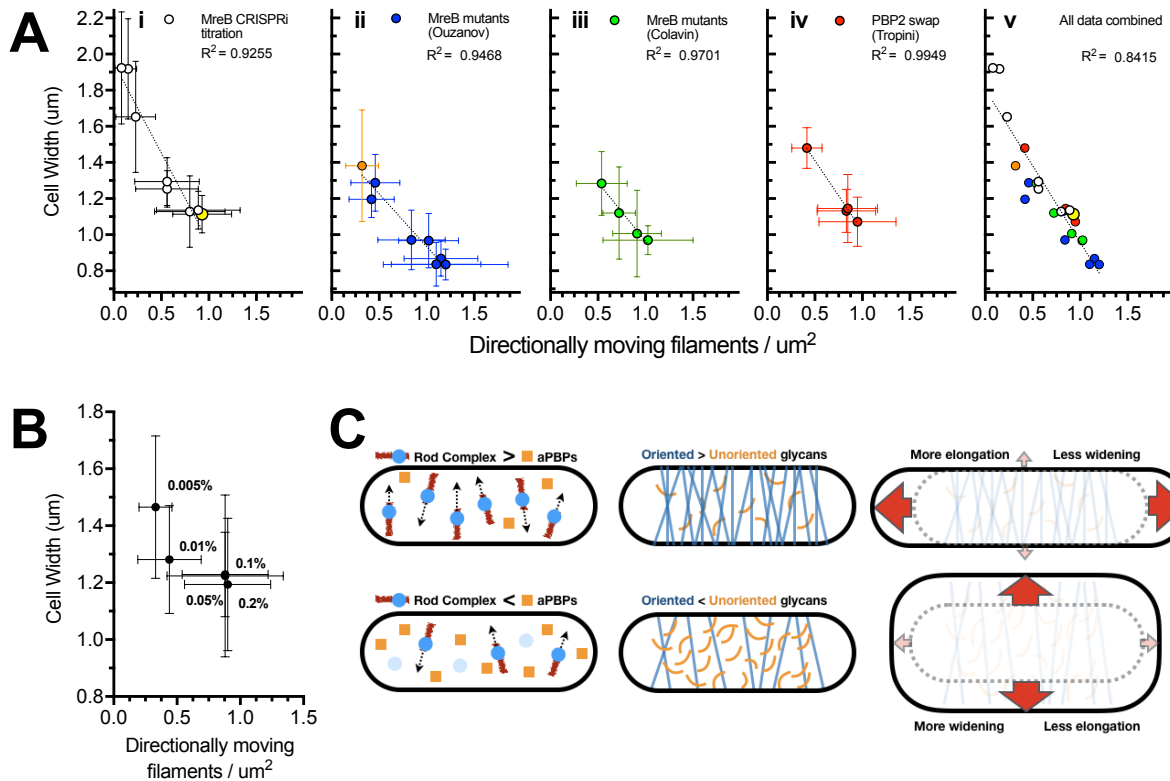
A. Cell width vs. density of directionally moving MreB filaments in different *E. coli* strains. (i) AV88 (186::P$_{tet}$-*dCas9*, *mreB*::*msfGFP-mreBsw*), allows the tunable expression of *mreB-msfGFPsw* by expressing various sgRNAs with different matches against msfGFP. Yellow indicates WT expression. **(ii)** mreB-SW-msfGFP mutant strains from Ouzounov et al., 2016. Orange indicates RM478 *(ΔrodZ, mreB(S14A)-msfGFPsw)* from Morgenstein et al., 2015. **(iii)** mreB-msfGFPsw mutants believed to change filament curvature from Colavin et al., 2018. **(iv)** msfGFP-mreB strains from Tropini et al., 2015, where *mrdA* is replaced with *mrdA* from other species. **(v)** All data from (i)-(iv) combined. See also **Movie SM4**. All values are detailed in **Table S1**.

B. Decreased cell width caused by increased RodZ expression correlates with an increased density of directionally moving MreB filaments. KC717 (*csrD::kan, mreB::msfGFP-mreB, ProdZ*◇*(frt araC PBAD)*) was grown at different arabinose concentrations (indicated on the graph), and filament density was calculated as in **Figure 3B**. See also **Movie SM5**.

C. Model for how the balance between aPBPs and the Rod system affects cell width. *Left* – When Rod complex activity (perhaps set by the number of MreB filaments) is high relative to that of aPBPs, sacculi have more circumferentially oriented material (*Center*) compared to when aPBP activity is greater. *Right* – As the amount of oriented material increases, the less elastic sacculi are more rigid across their width, but less rigid along their length. Being stretched by the internal turgor pressure, sacculi with greater Rod activity are better able to maintain their width, while stretching more along their length. In contrast, cells with reduced Rod activity have less circumferentially oriented glycans to reinforce their width, and thus expand more along their width.

19

666 # Supplemental Material for:

667

668 **Cell Diameter in *Bacillus subtilis* is Determined by the Opposing Actions of Two Distinct**
669 **Cell Wall Synthetic Systems**

670

671 Michael F. Dion[1,2,8], Mrinal Kapoor[1,2,8], Yingjie Sun[1,2,8], Sean Wilson[1,2] Joel Ryan[3,4], Antoine Vigouroux[5,6],
672 Sven van Teeffelen[5], Rudolf Oldenbourg[7], and Ethan C. Garner[1,2,4*]

673

674 [1] Department of Molecular and Cellular Biology, Harvard University, Cambridge, United States.
675 [2] Center for Systems Biology, Harvard University, Cambridge, United States.
676 [3] Department of Biology II, Ludwig-Maximilians-Universität München, Martinsried, Germany
677 [4] Physiology Course, Marine Biological Laboratory, Woods Hole, USA.
678 [5] Synthetic Biology Laboratory, Institut Pasteur, Paris, France.
679 [6] Microbial Morphogenesis and Growth Laboratory, Institut Pasteur, Paris, France.
680 [7] Marine Biological Laboratory, Bell Center, Woods Hole, United States
681 [8] These authors contributed equally to this work.
682
683 Corresponding Author: Ethan C. Garner
684 NW 445.20, Northwest Building, 52 Oxford Street, Cambridge, MA 02138
685 *E-mail: egarner@g.harvard.edu
686

687

688

689

690 **Supplemental figures.**
691
692 **Figure S1**
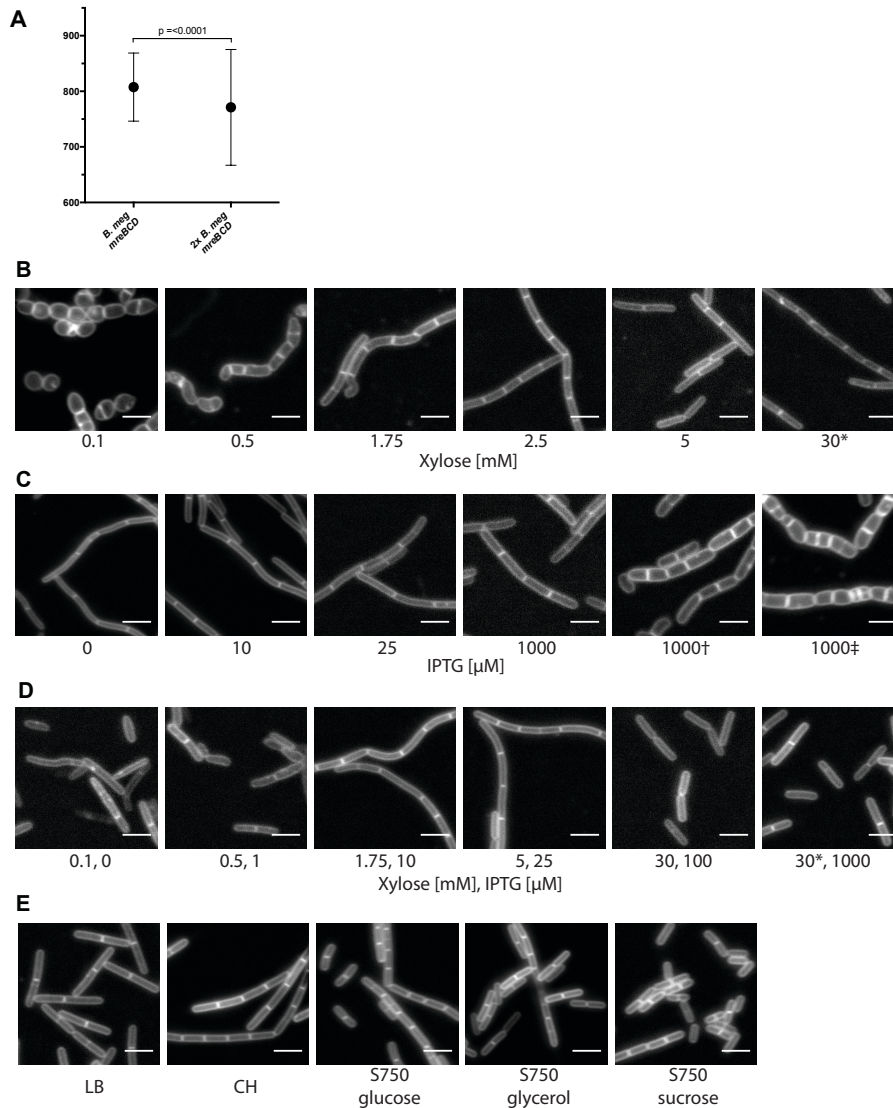
693
694 **A.** Zoomed view of the two rightmost distributions of widths in **Figure 1B**. Error bars are SD of the mean.
695
696 **B-D.** Cells were grown in CH media with the indicated concentrations of inducers during steady state growth, then stained with 0.5
697 µg/mL FM 5-95. Scale bars are 4 µm.
698
699 **B.** Images are of bMD545 (*amyE::Pxyl-mreBCD::erm, ΔmreBCD::spec)*, save the induction annotated * which is bMK355
700 (*amyE::Pxyl-mreBCD::erm*), containing a xylose inducible *mreBCD* in addition to the native *mreBCD*.
701
702 **C.** Images are of bMD598 (*yhdG::Pspank-ponA::cat, ΔponA::kan*), induced with the indicated amounts of IPTG, save the
703 inductions marked † and ‡ which are under stronger promoters than bMD598; † is bMD586 (*yhdG*::Phyperspank-*ponA*::*cat,*
704 *ΔponA::kan*), and ‡ is bMD554 (*yhdG*::Phyperspank-*ponA*::*cat*), containing an inducible *ponA* in addition to the native copy.
705
706 **D.** Images of bMD620 (*amyE*::Pxyl-*mreBCD*::*erm, ΔmreBCD::spec, yhdH*::Pspank-*ponA*::*cat, ΔponA::kan*) grown in CH, and
707 induced with the indicated amounts of IPTG and xylose. The image annotated * indicates bMD622 (*amyE::Pxyl-mreBCD::erm*
708 *yhdH::Pspank-ponA::cat ΔponA::kan*) containing a xylose-inducible *mreBCD* in addition to the native *mreBCD.*
709

21

710 **E.** Representative images of Py79 grown in indicated media, then stained with 0.5 µg/mL FM 5-95. Scale bars are 4 µm.
711
712 **Figure S3**
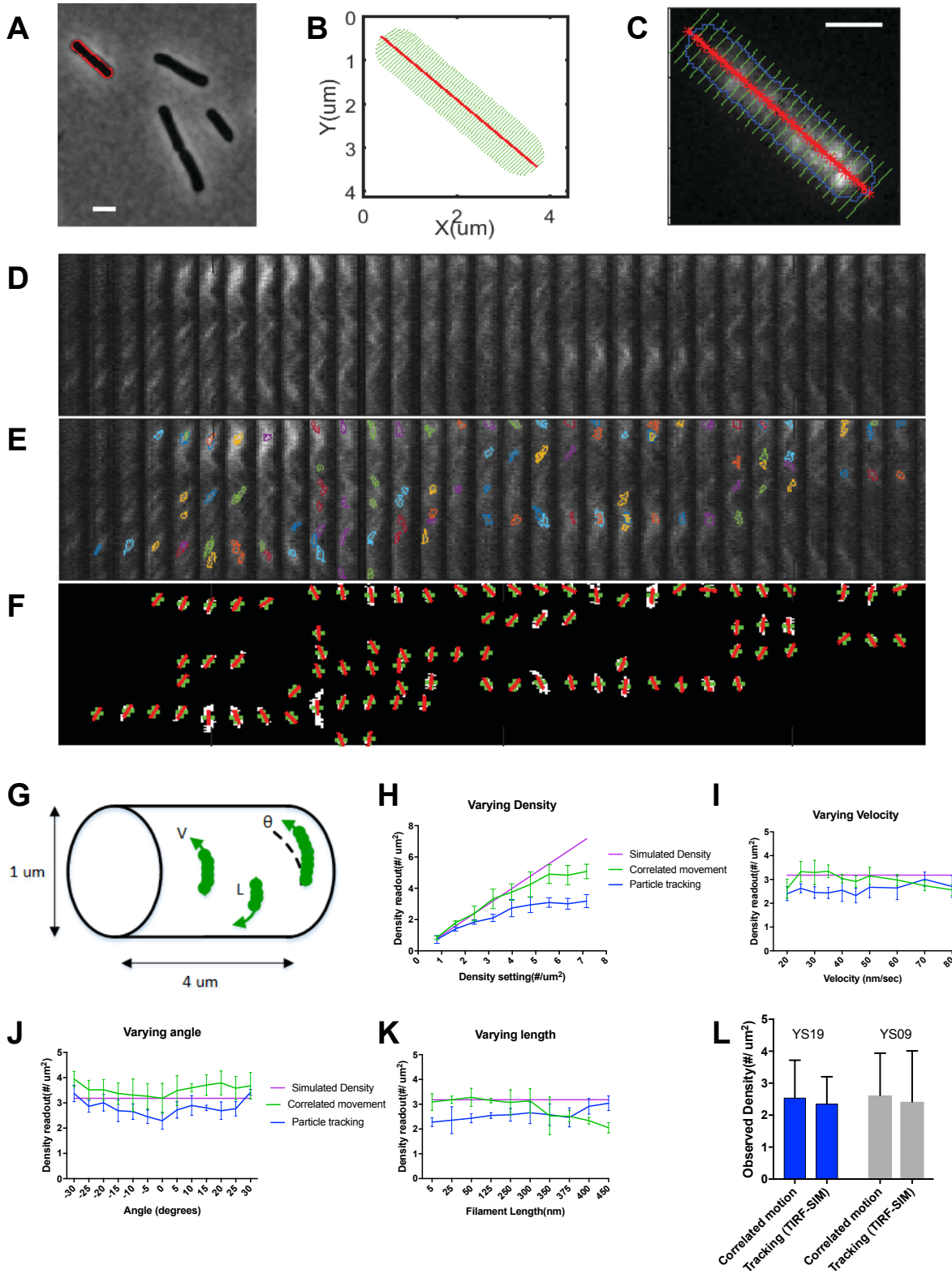
713

714 **A-F. Expanded description of the method used to determine directional filament density.** Cells expressing fluorescent MreB
715 fusions were imaged with TIRF for 120 seconds, followed by a single image in phase-contrast. From the phase-contrast images
716 (**(A) -** scale bar is 2 um**),** cells were segmented to determine their dimensions and midline **(B)**. The resulting segmentation mask
717 was used to create kymographs out of the fluorescence time-lapse data. **(C)** Shows the mask overlaid on a maximum intensity
718 projection of a TIRF time-lapse (red line indicates midline, green lines are the axis along which kymographs are drawn, scale bar is
719 2 um). Next, kymographs were created for each sequential row of pixels along the midline, and the kymographs from each row
720 were displayed side by side as in **(D)**. Next, objects within these kymographs were identified and segmented based on contour
721 analysis **(E)**, using adaptive thresholding. For each identified object, a set of properties [X, t, v, I] were measured. (X, t) are the
722 centroid of the object in the binary image (green crosses in **(F)**). X is the position of the filament along the cell width, and t is time,
723 corresponding to rows in the kymographs. Velocity (v) is calculated based on the diagonal slope of the object in the binary image
724 (red lines in **(E)**), and can be positive or negative depending on the direction of motion. Intensity (I) is the sum of the intensities of
725 all pixels in the object. Because each kymograph represents one row of pixels in the cell, and the signal from each particle can
726 span more than one pixel (65 nm) in width, the same filament can appear in several sequential kymographs (or rows in the original
727 image). In order to link the objects occurring in multiple rows together, each object in a given row [X_i] can be linked to
728 corresponding objects in the next row [X_{i+1}] or previous row [X_{i-1}] based on their time and velocity. Objects are only linked if they
729 have a velocity v +/-20 nm/sec of each other, and their peak time t is within 2 seconds; these objects are then counted as a single
730 filament. This also allows us to capture filaments moving at angles of up to +/- 30 degrees to the midline. Finally, the number of
731 counts occurring during the imaging interval is normalized based on the cell width and length (or total surface area π*width*length).
732
733 **G-J. Evaluation of filament density quantitation tested using simulations.**
734 **(G)** Schematic of the MreB data simulations. Simulations were run using custom MATLAB code, with the following parameters:
735 Maximum fluorescence intensity was 300 counts and noise was 10 (approximating the signal to noise conditions in our imaging).
736 The simulated cell had a width of 1 μm and a length of 4 μm. We tested the robustness of our tracking by varying one parameter
737 while the others were fixed at the following values: Filament density was 3.2/μm² (corresponding to 40 MreB filaments per cell),
738 filament velocity was 30 nm/sec, filament orientation was 0 degrees, and filament length was 250 nm. This data was tracked using
739 the correlated motion method detailed above. For comparison, we tracked the same simulated data with the linear motion LAP
740 tracker in Trackmate, with a low bar for calling a trace a directional motion (tracks longer than 6 frames with a displacement greater
741 than 250 nm). **(H)** Filament detection performance with respect to different filament density settings (from 0.8 to 7.2/um²,
742 corresponding to 10 - 90 MreB filaments per cell). **(I)** Filament detection with respect to filament angles (from -30 to 30 degrees).
743 **(J)** Filament detection with respect to different filament velocities (from 20 to 90 nm/sec). **(K)** Filament detection with respect to
744 different filament lengths (5 nm to 450 nm).
745
746 **L. Correlated motion analysis yields a similar density of directional filaments as tracking of MreB filaments imaged by**
747 **TIRF-SIM.** For this comparison, two different strains with natively expressed MreB fusions, YS09 (*mreB-mNeonGreen*) and YS19
748 (*mreB-SW-msfGFP*), were grown under the same conditions, and were analysed using two different imaging/analysis pipelines: 1)
749 As above, standard TIRFM imaging followed by correlated motion analysis, and 2) TIRF-SIM imaging, followed by tracking
750 filaments with particle tracking (using the same settings as in **(G)** above).
751
752
753
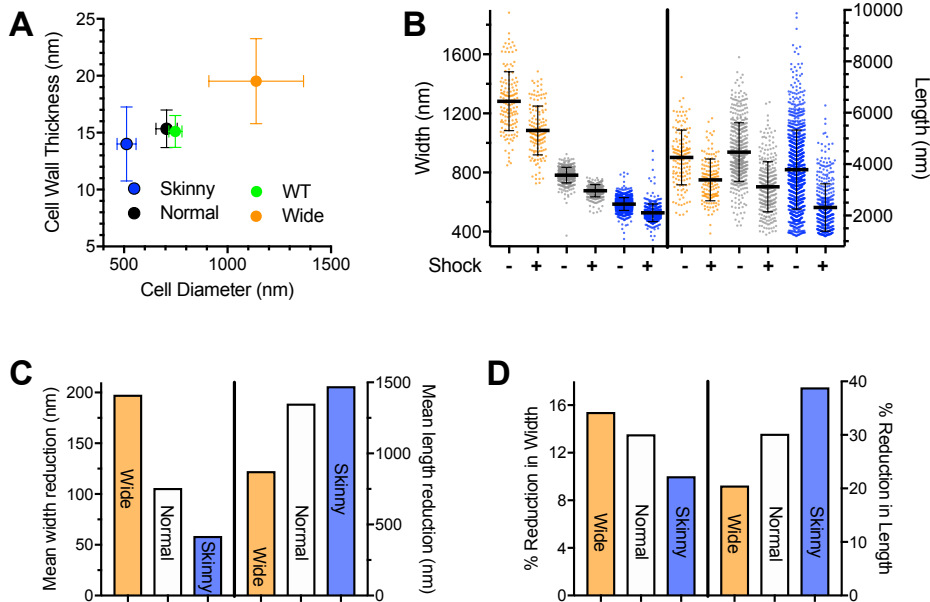
Figure S4

A. Cells, induced under identical conditions to **Figure 4B**, were fixed and stained with uranyl acetate, the block was cut in ultrathin sections, then imaged with transmission electron microscopy (TEM). The thickness of the cell wall was measured and plotted against cell diameter (also determined via TEM).

B. All data of the width (left) and length (right) of cells before and after osmotic shocks (orange = Wide, grey = Normal, blue = Skinny). Error bars are SD of the mean.

C Absolute and **D** percent reduction in width and length of labeled sacculi under each induction condition after osmotic shock.

Supplemental Movie Legends.

Movie S1 – Example single molecule movies of PBP2A-HaloTag (labeled with JF549[1]) at different *mreBCD* induction levels in bMK385 (*amyE::Pxyl-mreBCD::erm, ΔmreBCD, HaloTag-11aa-pbpA::cat*). Xylose concentrations are indicated in each panel. Frames are 300 msec apart.

Movie S2 – Z-stack of LC-PolScope images of sacculi purified from wild type Py79. (Left) Z-stack of the retardance of each plane. (Right) Color map of birefringence at each plane, with color wheel at upper left giving orientation reference. Z-steps were taken in 100 nm increments.

Movie S3 – Z-stack color map of birefringence of sacculi purified from strain bMD620 (*amyE::Pxyl-mreBCD::erm, ΔmreBCD, yhdG::Pspank-ponA::cat, ΔponA::kan*), where cells were induced to "Wide" (0.5 mM xylose, 0.1 mM IPTG) and "Normal" widths (5 mM xylose, 0.025 mM IPTG). Color wheel at upper left indicates orientation direction. Z-steps were taken in 100 nm increments.

Movie S4 – TIRF-SIM movies of different mreB-SW-msfGFP mutants. Cells were grown in LB at 37°C, then placed under an LB agar and imaged at 37°C. Frames are 1 sec apart. Scale bars are 1 um.

Movie S5 – TIRF-SIM movies of strain KC717(*mreB::msfGFP-mreB, ProdZ⬦(frt araC PBAD)*). Cells were grown for 5 hours in LB with the indicated arabinose concentrations, were placed under an LB agar pad and imaged at 37°C. Frames are 1 sec apart. Scale bars are 1 um.

24

Materials and Methods.

Media and culture conditions

For all experiments, unless otherwise noted, *B. subtilis* and *B. megaterium* were grown in casein hydrolysate (CH) medium (where indicated, xylose and/or isopropyl thiogalactoside (IPTG) was added), and *E. coli* strains were grown in lysogeny broth (LB) medium (where indicated, arabinose or anhydrotetracycline (ATc) was added), at 37°C with rotation. When pre-cultures reached exponential phase the next day, after overnight growth at 25°C, they were further diluted into fresh growth medium (and where indicated, with the specified concentrations of inducer) and were grown for at least 3 hours at 37°C with rotation, to an OD_{600} of ~0.3 to 0.7.

Sacculi purification

20 mL cultures were grown in 250 mL baffled flasks at 37°C with vigorous shaking, to an OD_{600} of ~0.5, were harvested and were centrifuged at 5,000 × g for 5 min at 4°C. Cell pellets were resuspended in 1 mL of ice-cold phosphate buffered saline (PBS), were centrifuged at 6,000 × g for 30 sec, were resuspended in 500 µL of PBS, and were killed by boiling in a water bath for 10 min. Cells were centrifuged at 6,000 × g for 2 min, were resuspended in 500 µL of PBS containing 5% sodium dodecyl sulfate (SDS), and were boiled in a water bath for 25 min; this was repeated once, except boiling was for 15 min. To remove the SDS, the samples were centrifuged at 6,000 × g for 2 min, and were resuspended in 500 µL of PBS; this was repeated 5 times. The cells were centrifuged at 6,000 × g for 2 min, were resuspended in 1 mL of 50 mM Tris-HCl, pH 7.5, containing 10 mM NaCl, and 2 mg of pronase from *Streptomyces griseus* (MilliporeSigma, MA), and were incubated at 60°C for 90 min with gentle shaking. To remove the pronase, the samples were boiled twice in PBS/5% SDS, followed by 6 rounds of washes in PBS, exactly as described in the steps above that precede the pronase treatment. The samples were centrifuged at 6,000 × g for 2 min, were resuspended in 1 mL of 25 mM Tris-HCl, pH 8.5, containing 0.5 M NaCl, 5 mM $MgCl_2$, and 100 U of salt-active nuclease (SAN) (ArticZymes, Norway), and were incubated at 4°C overnight with gentle mixing. To remove the SAN, the samples were boiled twice in PBS/5% SDS, followed by 6 rounds of washes in PBS, exactly as described in the steps above that precede the pronase treatment. The sacculi were centrifuged at 6,000 × g for 2 min, the supernatant was removed, and the pellets were stored at -80°C.

Polarization microscopy

Purified sacculi were resuspended in PBS and placed on ethanol-cleaned No. 1.5 coverslips under a cleaned glass slide. Polarization images were acquired on an inverted LC-PolScope mounted on a Nikon Ti-E equipped with a 60x/1.4NA Plan Apo oil immersion objective and oil condenser with matching NA, and a Hamamatsu Photonics Flash4 camera. Z-stacks in 100 nm steps were taken of each sample using 50 msec acquisitions of 546/12 nm light. All image acquisition, processing, and display, including colored display and line maps were prepared using the OpenPolScope Hardware Kit and plugins for ImageJ/Micro-Manager from OpenPolScope.org.

Calculation of retardance

Z-stacks of the computed total retardance for each slice were exported from OpenPolScope. These stacks were cropped at one frame above and beneath the focal planes of the top and the bottom of the cells, then projected into a single plane using ImageJ. To avoid getting high retardance values from the edge effects arising from the sides of the cell or the septa, we selected the retardance at the middle of the cell, using the average of line scans (5 pixels long and 3 wide) that were drawn down the center of cells, taking care to avoid edges and septa.

Transmission electron microscopy of cell wall thickness

Overnight cultures were diluted into fresh medium and grown to an OD_{600} of ~0.3 to 0.5. Cells were pelleted by centrifugation at 5,000 x g and fixed by resuspending in 100 mM MOPS pH 7 containing 2% paraformaldayde, 2.5% gluteraldehyde, and 1% DMSO overnight at 4°C. Cells were centrifuged at 5,000 x g and were washed 3 times with 100 mM MOPS pH 7. The pellet was stained with 2% osmium tetroxide in 100 mM MOPS for 1 hr, washed twice with deionized water, and stained overnight with 2% uranyl acetate. The pellet was washed twice with deionized water and dehydrated by washing once with 50% ethanol, once with 70% ethanol, once with 95% ethanol, and then three times with 100% (v/v) ethanol. Samples were prepared for resin infiltration by washing once with 50% ethanol, 50% propylene oxide (v/v) and then once with 100% propylene oxide. All wash steps were for 5 min. Infiltration of resin was

839 achieved by incubation with 50% Embed 812 (EMS, PA)/50% propylene oxide for 1 hr, followed by incubation with
840 67% Embed 812/33% propylene oxide for 1hr, and incubation with 80% Embed 812/20% propylene oxide for 1 hr.
841 Samples were then incubated twice with Embed 812 for 1 hr, followed by an overnight incubation in molds. The molds
842 were baked at 65°C for 18 hr before sectioning.
843
844 Serial ultrathin sections (80 nm) were cut with a Diatome diamond knife (EMS, PA) on a Leica Ultracut UCT (Leica
845 Microsystems, Germany) and collected on 200-mesh thin-bar formvar carbon grids. Sections were imaged on an FEI
846 Tecnai transmission electron microscope.
847
848 Cell wall thickness measurements were performed using a custom-built MATLAB (Mathworks, MA) script. Image
849 intensity profiles extracted from lines were drawn perpendicular to a user-input line defining the middle of the cell wall.
850 The distance between the two lowest points below a threshold within 40 nm of the middle of the cell wall was
851 measured as the cell wall thickness at ~30 points in each cell.
852
853 **Measurements of cell diameter**
854 Cultures grown to an OD_{600} of ~0.3 to 0.7 were stained with 0.5 µg/mL FM 5-95 (Thermo Fisher, MA) for 1 min, and
855 were concentrated by centrifugation at 6,000 x g for 30 sec. The cell pellet was resuspended in ~1/20 volume of
856 growth medium, and 3 µL was applied to ethanol-cleaned No. 1.5 coverslips under a 3% agarose pad containing
857 growth medium. Fluorescent cells were imaged with the top surface of the agarose pad exposed to air, in a chamber
858 heated to 37°C. Epifluorescence microscopy was performed using a Nikon Eclipse Ti equipped with a Nikon Plan Apo
859 λ 100×/1.4NA objective and an Andor camera. Cell contours and dimensions were calculated using the
860 Morphometrics software package [2].
861
862 **Measurements of single-cell growth rate**
863 Cultures grown to an OD_{600} below 0.3 were concentrated by centrifugation at 6,000 x g for 30 sec. The cell pellet was
864 resuspended in growth medium, and applied to No. 1.5 glass-bottomed dishes (MatTek Corp., MA). All cells were
865 imaged under a 2% agarose pad containing growth medium, with the top surface exposed to air, in a chamber heated
866 to 37°C. Phase-contrast microscopy was performed using a Nikon Eclipse Ti equipped with a Nikon Plan Apo λ
867 100×/1.4NA objective and an Andor camera. We used a custom-built package in MATLAB to perform segmentation
868 on phase-contrast time-lapse movies, then calculated the growth rate of the surface area of single *B. subtilis* chains.
869
870 **Measurements of bulk growth rate**
871 For cell culture measurements of growth rate, overnight cultures were diluted in fresh medium and grown for ~3 hr at
872 37°C to an OD_{600} of ~0.3 to 0.7. The cultures were diluted back to a calculated OD_{600} of 0.07 in 100-well microtiter
873 plates, and their growth rates were measured in a Bioscreen-C Automated Growth Curve Analysis System (Growth
874 Curves USA, NJ) plate reader, at 37°C with continuous shaking. Growth rates were calculated from OD_{600}
875 measurements that were recorded every 5 min for at least 6 hr.
876
877 **TIRF microscopy of Halo-PBP2A**
878 Cultures grown to an OD_{600} below 0.3 were labelled with 10 nM JF549 [3], and were concentrated by centrifugation at
879 6,000 x g for 30 sec. The cell pellet was resuspended in growth medium and applied to ethanol-cleaned No. 1.5
880 coverslips. All cells were imaged under a 2% agarose pad containing growth medium with the top surface exposed to
881 air, in a chamber heated to 37°C. TIRFM and phase-contrast microscopy were performed using a Nikon Eclipse Ti
882 equipped with a Nikon Plan Apo λ 100×/1.45NA objective and a Hamamatsu ORCA-Flash4.0 V2 sCMOS camera.
883 Fluorescence time-lapse images were collected by continuous acquisition with 300 msec exposures.
884
885 **Analysis of the density of MreB**
886 Phase images of bacteria were segmented using Morphometrics [4], and the width and length of each cell was
887 calculated. Next, the fluorescence time-lapses were analyzed based on the segmentation mask of the phase image
888 (**Figure S3C**). Filament counting was performed in several steps (**Figure S3**). First, kymographs were generated for
889 each row of pixels along the midline of the cell. Next, the kymographs for each row were placed side by side,
890 converting the TIRF time lapse data into a single 2D image (**Figure S3D**). To identify filaments in the kymograph,
891 closed contours were generated in the 2D image (**Figure S3E**). We only selected contours within a given size range

26

892 (0.04 µm^2 to 0.17 µm^2). For these contours, we calculated the total intensity (the sum of the intensities of the pixels in
893 the contour), the centroid, the velocity (calculated from the slope of the major axis line of the contour) (**Figure S3F**),
894 and time (from the centroid). Next, to identify cases where the same MreB filament appears in multiple sequential
895 kymographs, each object in a given kymograph is linked to a corresponding object in the next and previous
896 kymographs based on the above properties of the object (see **Figure S3F** for details). Finally, the counting is verified
897 manually by numbering each filament on the 2D image (**Figure 3A**). To test the performance of the filament counting,
898 we analyzed simulated data with different filament density, velocity, and orientation settings (**Figure S3**). All of the
899 image analyses were performed using MATLAB.
900
901 **Simulation of directionally moving MreB**
902 The Image Correlation Spectroscopy [5] MATLAB package was used for the simulation of MreB moving around the cell.
903 The following parameters were set for the MreB simulations: velocity, orientation, filament number and filament length.
904 The default velocity setting is 30 nm/sec and the default orientation is 0, which means MreB moves perpendicular to
905 the central axis. The default filament length is set to 250 nm and each MreB monomer is assumed to be 5 nm. The
906 cell width is set to 1 um and the cell length is set to 4 µm. The pixel size is 65 nm and the time interval is 1 sec, which
907 is the same as the TIRF imaging obtained with our Nikon Eclipse Ti equipped with a Hamamatsu ORCA-Flash4.0 V2
908 sCMOS camera. The particles are randomly distributed on the surface of the cell. Each simulation data point was
909 repeated 5 times for the counting analysis. To compare the correlated motion approach against particle tracking, we
910 counted the number of tracks observed after tracking the simulated data using the Linear Motion LAP tracker in FIJI [6]
911 with TrackMate v3.8 [7]. The threshold for spot size was 0.195 µm and the intensity threshold was 10 counts. The
912 search radius is 0.085 µm, the link radius is 0.085 µm, and the gap size is 1. All traces longer than 6 frames that had
913 moved more than 250 nm were considered directional motions.
914
915 **TIRF-SIM imaging of *E. coli* strains**
916 Cells were prepared as described in "Media and culture conditions". Cells were placed under an LB agarose pad, on a
917 cleaned No.1.5 coverslip, and imaged at 37°C. Live-cell SIM data were acquired as described previously [8] on a Zeiss
918 Axio Observer.Z1 inverted microscope outfitted for structured illumination. An Olympus 100×/1.49NA objective was
919 used instead of the Zeiss 1.45NA objective because the slightly larger NA of the Olympus objective gives higher
920 tolerance for placing the excitation beams inside the TIRF annulus. Data was acquired at 1 sec frame rates, with 20
921 msec exposures from a 488 nm laser for each rotation. TIRF-SIM images were reconstructed as described previously
922 [8].
923
924 **TIRF-SIM imaging of *B. subtilis* strains**
925 Cells were prepared as described in "Media and culture conditions". Cells were placed under a CH agarose pad in a
926 No. 1.5 glass-bottomed dish (MatTek Corp., MA) for imaging. Images were collected on a DeltaVision OMX SR Blaze
927 system in TIRF mode, using an Edge 5.5 sCMOS camera (PCO AG, Germany) and a 60x objective. 75 msec
928 exposures from a 488 nm diode laser were used for each rotation. Spherical aberration was minimized using
929 immersion oil matching. Raw images were reconstructed using SoftWoRx (GE Healthcare, MA) software.
930
931 **Particle tracking of JF549-Halo-PBP2A**
932 Particle tracking was performed using the software package FIJI [6] and the TrackMate v3.8 [7] plugin. For calculation of
933 particle velocity, the scaling exponent α, and track orientations relative to the midline of the cell, only tracks persisting
934 for 7 frames or longer were used. Particle velocity for each track was calculated from nonlinear least squares fitting
935 using the equation $MSD(t) = 4Dt + (vt)^2$, where MSD is mean squared displacement, t is time interval, D is the
936 diffusion coefficient, and v is speed. The maximum time interval used was 80% of the track length. To filter for
937 directionally moving tracks, we discarded those with a velocity lower than 0.01 nm/sec. Tracks were also excluded if
938 the R^2 for log MSD versus log t was less than 0.95, indicating a poor ability to fit the MSD curve.
939
940 **Osmotic shock experiments**
941 Overnight, exponentially growing cultures (as described in "Media and culture conditions") were diluted into fresh CH
942 medium, grown at 37°C to an OD_{600} of 0.1 to 0.2, then stained by growing in 100 µM Alexa Fluor 488-D-Lysine-NH2
943 for 1 hr. Without washing, cells were then loaded into a CellASIC microfluidic flow cell (MilliporeSigma, MA) pre-
944 conditioned with media and washed in the chamber via channels 6 and 5. Media in channel 6 was replaced with 5 M

27

945 NaCl, and the flow cell was resealed and imaged immediately. After collecting images across the whole chip pre-
946 shock, 5 M NaCl was flowed into the chip via channel 6 and imaged immediately.
947
948 **Alexa Fluor 488-D-Lysine-NH2**
949 Alexa Fluor 488-D-Lysine-NH2 was synthesized as in Lebar et al., 2014. Briefly, Boc-D-Lys(Cbz)-OH (Bachem,
950 Switzerland) was reacted with carbonyldiimidazole (CDI) (MilliporeSigma, MA) in dimethylformamide (DMF) for 1.5 hr,
951 then aqueous ammonia was added and stirred for 6 hr to form the carboxamide Boc-D-Lys(Cbz)-NH2. The Cbz
952 protecting group was removed by catalytic hydrogenation (20% Pd(OH)2/C) in methanol. The product, Boc-D-Lys-
953 NH2, was reacted with CDI in DMF for 1.5 hr, then Alexa Fluor 488 carboxylic acid in DMF was added and reacted for
954 6 hr to yield Boc-D-Lys(Alexa Fluor 488)-NH2. The Boc protecting group was removed by stirring in neat
955 trifluoroacetic acid (TFA) for 30 min. The reaction was stopped by dropwise addition of TFA solution to ice-cold ether.
956 The precipitate was then HPLC-purified to obtain Alexa Fluor 488-D-Lysine-NH2.
957
958 **CRISPRi titration of MreB expression**
959 We used complementarity-based CRISPR knockdown to titrate the MreB expression level in *E. coli*. The degree of
960 MreB-SW-msfGFP repression is controlled by introducing mismatches between the guide RNA and the target DNA [9].
961 The repression strength can be tuned by modulating spacer complementarity to msfGFP using different numbers of
962 mismatches. To repress msfGFP using CRISPR knockdown, we placed the dCas9 cassette under the control of a
963 Ptet promoter and different plasmids to target msfGFP. We induced dCas9 at a constant high level with 100 ng/ml of
964 ATc and changed the degree of guide RNA complementarity with different plasmids. For pcrRNA plasmid we use four
965 different guide RNAs with 10, 11, 14, and 20 bp of complementarity. For pAV20 plasmid we use four different guide
966 RNAs with 5, 10, 14, and 20 bp of complementarity. The cells were grown and imaged in LB containing 50 ug/ml
967 kanamycin.
968
969 **Protein extraction and labelling**
970 Cell cultures were grown to an OD_{600} of ~0.4 to 0.6 (cell amounts were normalized by harvesting the equivalent of 3
971 mL of culture at an OD_{600} of 0.5). Cells were centrifuged at 6,000 × *g* for 30 sec, washed once in 1 mL of ice-cold 20
972 mM Tris-HCl, pH 7.5, and 10 mM EDTA (TE), were resuspended in 100 µL of TE, and were killed by boiling in a water
973 bath for 10 min. All samples were frozen at -80°C overnight (or up to 1 week). Thawed samples were digested with 50
974 µg of lysozyme (Thermo Fisher, MA) in the presence of 1 mM PMSF, at 37°C for 15 min.
975
976 Protein extraction was achieved utilizing a Covaris S220 ultrasonicator (Covaris, MA), under denaturing conditions
977 upon the addition of urea-based Protein Extraction Buffer DF (Covaris, MA), followed by ice-cold methanol/chloroform
978 precipitation. Proteins were digested with trypsin (Promega, WI). Each resulting peptide mixture was labeled with one
979 of a set of up to eleven isotopic tandem mass tags (TMTs) (Thermo Fisher, MA).
980
981 **Peptide fractionation and mass spectrometry**
982 Equal amounts of each TMT-labelled sample were combined and fractionated by electrostatic repulsion-hydrophobic
983 interaction chromatography, on an Agilent (Santa Clara, CA) 1200 HPLC system using a PolyWAX LP 200 x 2.1 mm,
984 5 µm, 300Å column (PolyLC, MD). Peptides were separated across a 70 min gradient from 0% of "buffer A" (90%
985 acetonitrile, 0.1% acetic acid) to 75% of "buffer B" (30% acetonitrile, 0.1% formic acid), with 20 fractions collected over
986 time. Each fraction was dried in a SpeedVac (Eppendorf, Germany) and resuspended in 0.1% formic acid before
987 injection to a mass spectrometer.
988
989 LC-MS/MS was performed on a Thermo Orbitrap Elite (Thermo Fisher, MA) mass spectrometer equipped with a
990 Waters nanoACQUITY HPLC pump (Waters Corp., MA). Peptides were separated on a 150 µm inner diameter
991 microcapillary trapping column packed with ~3 cm of C18 Reprosil 5 µm, 100 Å resin (Dr. Maisch GmbH, Germany),
992 followed by an analytical column packed with ~20 cm of Reprosil 1.8 µm, 200 Å resin. Separation was achieved by
993 applying a gradient of 5–27% acetonitrile in 0.1% formic acid, over 90 min at 200 nl/min. Electrospray ionization was
994 achieved by applying a voltage of 2 kV using a home-made electrode junction at the end of the microcapillary column
995 and sprayed from fused-silica PicoTips (New Objective, MA). The Orbitrap instrument was operated in data-
996 dependent mode for the mass spectrometry methods. The mass spectrometry survey scan was performed in the
997 Orbitrap in the range of 410 –1,800 m/z at a resolution of 12×10^4, followed by the selection of the twenty most

28

998   intense ions for HCD-MS2 fragmentation using a precursor isolation width window of 2 m/z, AGC setting of 50,000,
999   and a maximum ion accumulation of 200 msec. Singly-charged ion species were not subjected to HCD fragmentation.
1000   Normalized collision energy was set to 37 V and an activation time of 1 msec. Ions in a 10 ppm m/z window around
1001   ions selected for MS2 were excluded from further selection for fragmentation for 60 sec.
1002
1003   Mass spectrometry analysis: Raw data were submitted for analysis in Proteome Discoverer 2.1.0.81 (Thermo
1004   Scientific) software. Assignment of MS/MS spectra was performed using the Sequest HT algorithm by searching the
1005   data against a protein sequence database that including all entries from *B. subtilis* (UniProt proteome ID
1006   UP000018540) and other known contaminants such as human keratins and common lab contaminants. Sequest HT
1007   searches were performed using a 15 ppm precursor ion tolerance and required each peptide's N- and C-termini to
1008   adhere with trypsin protease specificity, while allowing up to two missed cleavages. TMT tags on peptide N-termini
1009   and lysine residues (+229.162932 Da) were set as static modifications while methionine oxidation (+15.99492 Da)
1010   was set as a variable modification. An MS2 spectra assignment false discovery rate (FDR) of 1% on protein level was
1011   achieved by applying the target-decoy database search. Filtering was performed using Percolator (64-bit version [10]).
1012   For quantification, a 0.02 m/z window centered on the theoretical m/z value of each of the TMT reporter ions and the
1013   intensity of the signal closest to the theoretical m/z value was recorded. Reporter ion intensities were exported in a
1014   results file of the Proteome Discoverer 2.1 search engine in Microsoft Excel format. The total signal intensity across all
1015   peptides quantified was summed for each TMT channel, and all intensity values were adjusted to account for
1016   potentially uneven TMT-labelling and/or sample handling variance for each labelled channel. For our final relative
1017   protein quantitation analysis, all contaminants from the database search were removed from the results, and only the
1018   remaining *B. subtilis* proteins were used to re-normalize all protein abundances.
1019
1020

29

Strain construction

bMD277 containing *amyE::Pxyl-mreBCD, minCD (B. megaterium)::erm* was generated upon transformation of Py79 with a five-piece Gibson assembly reaction[11], that contained the following PCR products. (1) A 1228 bp fragment containing sequence upstream of the *amyE* locus (amplified from Py79 genomic DNA using primers oMD191 and oMD108); (2) the 1673 bp erythromycin-resistance cassette *loxP-erm-loxP* (amplified from pWX467 [gift of D. Rudner] using primers oJM028 and oJM029); (3) a 1532 bp fragment containing the *xylR* gene, and the *PxylA* promoter with an optimized ribosomal binding sequence (amplified from pDR150 [gift of D. Rudner] using primers oMD73 and oMD226); (4) a 4106 bp fragment containing the *mreB, mreC, mreD, minC* and *minD* alleles of the *B. megaterium mreB* operon (amplified from strain QMB 1551 (ATCC 12872) genomic DNA using primers oMD227 and oMD228); and (5) a 1216 bp fragment containing the *amyE* terminator, and sequence downstream of the *amyE* locus (amplified from Py79 genomic DNA using primers oMD196 and oMD197).

bMD465 harboring *amyE::Pxyl-mreBCD, minCD (B. megaterium)::erm, mreBCD, minC,D::spec (B. megaterium)* was generated upon transformation of bMD277 with a four-piece Gibson assembly reaction, that contained the following PCR products. (1) A 1275 bp fragment containing sequence upstream of the *mreB* gene (amplified from Py79 genomic DNA using primers oMD96 and oMD308); (2) a 4121 bp fragment containing the *mreB, mreC, mreD, minC* and *minD* alleles of the *B. megaterium mreB* operon (amplified from strain QMB 1551 (ATCC 12872) genomic DNA using primers oMD313 and oMD314); (3) the 1274 bp spectinomycin-resistance cassette *loxP-spec-loxP* (amplified from pWX466 [gift of D. Rudner] using primers oJM028 and oJM029); and (4) a 1152 bp fragment containing sequence downstream of the *minD* gene (amplified from Py79 genomic DNA using primers oMD300 and oMD315).

bMK355 harboring *amyE::Pxyl-mreBCD::erm* was built identical to bMD277, except that PCR product (4) was instead a 2493 bp fragment containing the *mreB*, *mreC*, and *mreD* alleles of the *B. subtilis mreB* operon (amplified from Py79 genomic DNA using primers oMD334 and oMK221).

bMD543 containing *amyE::Pxyl-mreBCD::erm, ΔmreBCD, ΔminCD::cat* was generated upon transformation of bMK355 with a three-piece Gibson assembly reaction, that contained the following PCR products. (1) A 1305 bp fragment containing sequence upstream of the *mreB* gene (amplified from Py79 genomic DNA using primers oMD96 and oMD298); (2) the 1139 bp chloramphenicol-resistance cassette *loxP-cat-loxP* (amplified from pWX465 [gift of D. Rudner] using primers oJM028 and oJM029); and (3) a 1215 bp fragment containing sequence downstream of the *minD* gene (amplified from Py79 genomic DNA using primers oMD299 and oMD300).

bMD545 containing *amyE::Pxyl-mreBCD::erm, ΔmreBCD, PmreB-minC,D::spec* was generated upon transformation of bMD543 with a four-piece Gibson assembly reaction, that contained the following PCR products. (1) A 1305 bp fragment containing sequence upstream of the *mreB* gene (amplified from Py79 genomic DNA using primers oMD96 and oMD379); (2) a 1582 bp fragment containing the *minC* and *minD* genes, and the *minD* terminator of the *mreB* operon (amplified from Py79 genomic DNA using primers oMD380 and oMD381); (3) the 1274 bp spectinomycin-resistance cassette *loxP-spec-loxP* (amplified from pWX466 using primers oJM028 and oJM029); and (4) a 1215 bp fragment containing sequence downstream of the *minD* gene (amplified from Py79 genomic DNA using primers oMD300 and oMD382).

bMD599 harboring *ΔponA::kan* was generated upon transformation of Py79 with a three-piece Gibson assembly reaction, that contained the following PCR products. (1) A 1329 bp fragment containing sequence upstream of the *ponA* gene (amplified from Py79 genomic DNA using primers oMK001 and oMK002); (2) the 1577 bp kanamycin-resistance cassette *loxP-kan-loxP* (amplified from pWX470 [gift of D. Rudner] using primers oJM028 and oJM029); and (3) a 1313 bp fragment containing sequence downstream of the *ponA* gene (amplified from Py79 genomic DNA using primers oMK005 and oMK006).

bMK005 containing *ΔponA::cat* was built identical to bMD599, except that PCR product (2) was instead the 1139 bp chloramphenicol-resistance cassette *loxP-cat-loxP* (amplified from pWX465 using primers oJM028 and oJM029).

1073 **bMD554** containing *yhdG::Phyperspank-ponA::cat* was generated upon transformation of Py79 with a five-piece
1074 Gibson assembly reaction, that contained the following PCR products. (1) A 1219 bp fragment containing sequence
1075 upstream of the *yhdH* gene (amplified from Py79 genomic DNA using primers oMD328 and oMD367), (2) the 1139 bp
1076 chloramphenicol-resistance cassette *loxP-cat-loxP* (amplified from pWX465 using primers oJM028 and oJM029); (3) a
1077 1895 bp fragment containing the *lacI* gene, and the *Phyperspank* promoter with an optimized ribosomal binding
1078 sequence (amplified from pDR111 [gift of D. Rudner] using primers oMD232 and oMD234); (4) a 2799 bp fragment
1079 containing the *ponA* coding region (amplified from Py79 genomic DNA using primers oMD365 and oMK370); and (5) a
1080 1252 bp fragment containing the *yhdG* terminator, and sequence downstream of the *yhdG* gene (amplified from Py79
1081 genomic DNA using primers oMD371 and oMD372).
1082
1083 **bMD586** harboring *yhdG::Phyperspank-ponA::cat*, *ΔponA::kan* was generated upon transformation of bMD554 with
1084 genomic DNA from bMD599.
1085
1086 **bMD594** harboring *yhdG::Pspank-ponA::cat* was built identical to bMD554, except that PCR product (1) was instead a
1087 1287 bp fragment made with primers oMD328 and oMD329; and PCR product (3) containing the *Pspank* promoter
1088 was instead amplified from pDR110 (gift of D. Rudner).
1089
1090 **bMD598** containing *yhdG::Pspank-ponA::cat*, *ΔponA::kan* was generated upon transformation of bMD594 with
1091 genomic DNA from bMD599.
1092
1093 **bMD619** containing *amyE::Pxyl-mreBCD::erm, ΔmreBCD, PmreB-minCD::spec*, *yhdG::Pspank-ponA::cat* was
1094 generated upon transformation of bMD545 with genomic DNA from bMD594.
1095
1096 **bMD620** containing *amyE::Pxyl-mreBCD::erm, ΔmreBCD, PmreB-minCD::spec*, *yhdG::Pspank-ponA::cat*, *ΔponA::kan*
1097 was generated upon transformation of bMD619 with genomic DNA from bMD599.
1098
1099 **bMD622** harboring *amyE::Pxyl-mreBCD::erm*, *yhdG::Pspank-ponA::cat*, *ΔponA::kan* was generated upon
1100 transformation of bMD598 with genomic DNA from bMK355.
1101
1102 **bMD556** harboring *yhdG::Phyperspank-rodA::cat* was built identical to bMD554, except that PCR product (4) was
1103 instead a 1236 bp fragment containing the *rodA* coding region (amplified from Py79 genomic DNA using primers
1104 oMD364 and oMK369).
1105
1106 **bMD580** containing *yhdG::Phyperspank-rodA::cat*, *ΔrodA::kan* was generated upon transformation of bMD556 with a
1107 three-piece Gibson assembly reaction, that contained the following PCR products. (1) A 1265 bp fragment containing
1108 sequence upstream of the *rodA* gene (amplified from Py79 genomic DNA using primers oMD388 and oMD389); (2)
1109 the 1577 bp kanamycin-resistance cassette *loxP-kan-loxP* (amplified from pWX470 using primers oJM028 and
1110 oJM029); and (3) a 1258 bp fragment containing sequence downstream of the *rodA* gene (amplified from Py79
1111 genomic DNA using primers oMD386 and oMD387).
1112
1113 **bMD592** harboring *Pxyl-rodA::erm* was generated upon transformation of Py79 with a four-piece Gibson assembly
1114 reaction, that contained the following PCR products. (1) A 1265 bp fragment containing sequence upstream of the
1115 *rodA* gene (amplified from Py79 genomic DNA using primers oMD388 and oMD389); (2) the 1673 bp erythromycin-
1116 resistance cassette *loxP-erm-loxP* (amplified from pWX467 using primers oJM028 and oJM029); (3) a 1532 bp
1117 fragment containing the *xylR* gene, and the *PxylA* promoter with an optimized ribosomal binding sequence (amplified
1118 from pDR150 using primers oMD73 and oMD226); and (4) a 1271 bp fragment containing the *rodA* coding region
1119 (amplified from Py79 genomic DNA using primers oMD394 and oMD395).
1120
1121 **bMD627** containing *Pxyl-rodA::erm*, *ΔpbpH::spec* was generated upon transformation of bMD592 with genomic DNA
1122 from bDR2487.
1123

31

bMD563 containing *yhdG::Phyperspank-pbpA::cat* was built identical to bMD554, except that PCR product (4) was instead a 2204 bp fragment containing the *pbpA* coding region (amplified from Py79 genomic DNA using primers oMD316 and oMK368).

bMD573 harboring *yhdG::Phyperspank-pbpA::cat*, *ΔpbpH::spec* was generated upon transformation of bMD563 with genomic DNA from bRB776.

bMD574 harboring *yhdG::Phyperspank-pbpA::cat*, *ΔpbpA::erm*, *ΔpbpH::spec* was generated upon transformation of bMD573 with genomic DNA from bRB776.

bMD590 containing *Pxyl-pbpA::erm* was generated upon transformation of Py79 with a four-piece Gibson assembly reaction, that contained the following PCR products. (1) A 1233 bp fragment containing sequence upstream of the *pbpA* gene (amplified from Py79 genomic DNA using primers oMD75 and oMD125); (2) the 1673 bp erythromycin-resistance cassette *loxP-erm-loxP* (amplified from pWX467 using primers oJM028 and oJM029); (3) a 1537 bp fragment containing the *xylR* gene, and the *PxylA* promoter containing the *pbpA* ribosomal binding sequence (amplified from pDR150 using primers oMD73 and oMD72); and (4) a 1230 bp fragment containing the *pbpA* coding region (amplified from Py79 genomic DNA using primers oMD393 and oMD68).

bMD597 harboring *Pxyl-pbpA::erm*, *ΔpbpH::spec* was generated upon transformation of bMD590 with genomic DNA from bDR2487.

bMD557 containing *amyE::Pxyl-mreBCD::erm*, *yhdG::Phyperspank-rodA::cat* was generated upon transformation of bMK355 with genomic DNA from bMD556.

bMD571 harboring *amyE::Pxyl-mreBCD::erm*, *yhdG::Phyperspank-pbpA::cat* was generated upon transformation of bMK355 with genomic DNA from bMD563.

bMD631 containing *yhdG::Pspank-pbpA::phleo*, *ΔpbpH::spec*, *ΔpbpA::cat*, *Pxyl-rodA::erm* was generated upon transformation of bRB773 with genomic DNA from bMD592.

bYS201 harboring *HaloTag-11aa-pbpA::cat* was generated upon transformation of Py79 with a four-piece Gibson assembly reaction, that contained the following PCR products. (1) A 1233 bp fragment containing sequence upstream of the *pbpA* gene (amplified from Py79 genomic DNA using primers oMD75 and oMD125); (2) the 1139 bp chloramphenicol-resistance cassette *loxP-cat-loxP* (amplified from pWX465 using primers oJM028 and oJM029); (3) a 962 bp fragment containing the native *pbpA* promoter, and *B. subtilis*-optimized coding sequence of the HaloTag protein (amplified from double-stranded DNA custom-ordered from DNA 2.0/ATUM [Newark, CA] using primers oYS598 and oYS599); and (4) a 1229 bp fragment containing the *pbpA* coding region (amplified from Py79 genomic DNA using primers oMD68 and oMD69).

bMK385 harboring *amyE::Pxyl-mreBCD::erm*, *ΔmreBCD*, *PmreB-minCD::spec*, *HALO-11aa-pbpA::cat* was generated upon transformation of bMD545 with genomic DNA from bYS201.

bYS19 containing *mreB-SW-msfGFP* was generated upon transformation of bMD88 [12] with a three-piece Gibson assembly reaction that contained the following PCR products. (1) A 898 bp PCR fragment containing sequence upstream of the *mreB* gene (amplified from Py79 genomic DNA using primers oMD134 and oYS34); (2) a 774 bp fragment containing *B. subtilis*-optimized coding sequence of the msfGFP fluorescent protein (amplified from plasmid DNA custom-ordered from DNA 2.0/ATUM [Newark, CA] using primers oYS35 and oYS36); and (3) a 1629 bp fragment containing sequence downstream of the *mreB* gene (amplified from Py79 genomic DNA using primers oYS37 and oMD116). This strain is markerless, and selection was in the presence of 0.5% glucose for colonies that no longer required xylose for viability.

32

1175 **bYS977** harboring *amyE::Pxyl-mreB-SW-msfGFP, mreCD::erm,* was built identical to bMD277, except that PCR
1176 product (4) was instead a 3234 bp fragment containing *mreB-SW-msfGFP*, *mreC*, and *mreD*, amplified from bYS19
1177 genomic DNA using primers oMD334 and oMK221).
1178
1179 **bYS979** containing *amyE::Pxyl-mreB-SW-msfGFP, mreCD::erm, ΔmreBCD, ΔminCD::cat* was generated upon
1180 transformation of bYS977 with genomic DNA from bMD543.
1181
1182 **bYS981** harboring *amyE::Pxyl-mreB-SW-msfGFP, mreCD::erm, ΔmreBCD, PmreB-minC,D::spec* was generated
1183 upon transformation of bYS979 with genomic DNA from bMD545.
1184
1185 **AV88** containing *186::Ptet-dCas9, mreB-SW-msfGFP* was obtained by transduction of strain LC69 with a P1 phage
1186 lysate obtained from strain NO50, and subsequent excision of the kanamycin resistance cassette by transient
1187 expression of a flippase. To make the plasmids expressing single-guide RNAs, the psgRNA plasmid was amplified
1188 three times with primers pairs V162/V165, V163/V166 and V164/V167. The three generated fragments were
1189 assembled together by Gibson assembly to obtain the pAV20 vector. To insert the anti-GFP single-guide RNAs into
1190 this vector, we annealed and phosphorylated the following pairs of oligonucleotides: V275/V283 for G5; V274/V282
1191 for G10; V273/V281 for G14; and V272/V280 for G20. These were then inserted in pAV20 by restriction cloning with
1192 *Bsa*I. As pAV20 carries two sgRNA insertion sites, a non-targeting oligonucleotide pair (V279/V287) was inserted into
1193 a second site during the same reaction.

1194

1195

Statistics.

All P-values are reported in figures. P-values were calculated in GraphPad Prism using the Mann-Whitney test with a two-tailed P value. Means, SD, and N for all data points are reported in table S1.

Table S1 – Data summary and statistics.

A - Figure 1.

Panel	Strain	condition.	parameter	Value	SD	N
B	Py79		width(nm)	754.70	81.19	466
B	*B. megaterium*		width(nm)	1377.88	98.09	337
B	bMD465	1% glucose	width(nm)	807.52	61.24	267
B	bMD465	30 mM xylose	width(nm)	771.20	104.12	135
C	bMD545	0.1 mM xylose	width(nm)	1533.00	247.40	501
C	bMD545	0.5 mM xylose	width(nm)	1179.00	165.50	466
C	bMD545	1 mM xylose	width(nm)	1059.00	145.70	395
C	bMD545	1.75 mM xylose	width(nm)	930.80	83.53	282
C	bMD545	2.5 mM xylose	width(nm)	807.80	90.69	461
C	bMD545	5 mM xylose	width(nm)	735.00	80.10	269
C	bMD545	30 mM xylose	width(nm)	722.10	60.64	619
C	bMK355	30 mM xylose	width(nm)	696.50	85.40	276
D	bMD599		width(nm)	575.90	97.00	174
D	bMD598	0 M IPTG	width(nm)	580.60	60.57	148
D	bMD598	1 µM IPTG	width(nm)	601.00	68.93	141
D	bMD598	10 µM IPTG	width(nm)	651.40	74.63	742
D	bMD598	25 µM IPTG	width(nm)	767.80	91.60	309
D	bMD598	100 µM IPTG	width(nm)	825.00	78.83	361
D	bMD598	1000 µM IPTG	width(nm)	868.70	78.53	654
D	bMD586	25 µM IPTG	width(nm)	935.30	106.00	332
D	bMD586	50 µM IPTG	width(nm)	1031.30	97.14	381
D	bMD586	100 µM IPTG	width(nm)	1149.45	119.40	133
D	bMD586	1000 µM IPTG	width(nm)	1283	137.8	619
D	bMD554	1000 µM IPTG	width(nm)	1519	169.4	276
E	bMD620	0.1 mM xylose, 0 M IPTG	width(nm)	786.00	159.30	452
E	bMD620	0.5 mM xylose, 1 µM IPTG	width(nm)	744.50	137.90	265
E	bMD620	2.5 mM xylose, 10 µM IPTG	width(nm)	754.40	76.76	522
E	bMD620	5 mM xylose, 25 µM IPTG	width(nm)	749.00	73.91	288
E	bMD620	30 mM xylose, 100 µM IPTG	width(nm)	784.80	76.63	589
E	bMD622	30 mM xylose, 1000 µM IPTG	width(nm)	773.30	58.09	665
F	Py79	LB	width(nm)	770.50	44.09	590
F	Py79	CH	width(nm)	754.70	81.19	466
F	Py79	S750 glucose	width(nm)	767.49	78.52	389
F	Py79	S750 Glycerol	width(nm)	756.90	70.21	596
F	Py79	S750 Sucrose	width(nm)	761.51	63.79	360

34

1205

1206 ## B - Figure 2

Panel	Strain	Conditions	parameter	Value	SD	N
A	bMD592	0.1mM xyl	width(nm)	1113	221.8	387
A	bMD592	0.5mM xyl	width(nm)	959.8	156.6	389
A	bMD592	1mM xyl	width(nm)	753.2	106.6	370
A	bMD592	30mM xyl	width(nm)	964.2	77.79	466
A	bMD580	1mM IPTG	width(nm)	1133	110.8	555
A	bMD556	1mM IPTG	width(nm)	1323	155.5	788
A	bMD598	0.1mM xyl	width(nm)	1081	206.5	455
A	bMD599	0.5mM xyl	width(nm)	927.6	117.8	442
A	bMD600	1mM xyl	width(nm)	749.3	77.61	135
A	bMD601	30mM xyl	width(nm)	782	52.83	91
A	bMD602	1mM IPTG	width(nm)	790.1	66.96	288
A	bMD603	1mM IPTG	width(nm)	795.1	59.96	443
B	bMD627	0.025mM xyl	width(nm)	1381	334.7	92
B	bMD627	1mM xyl	width(nm)	756.4	52.33	983
B	bMD627	30mM xyl	width(nm)	793.4	62.71	414
B	bMD631	025µM xyl, 15 IPTG	width(nm)	1346	371.4	79
B	bMD631	1mM xyl, 15µM IPTG	width(nm)	757.9	55.22	441
B	bMD631	30mM xyl 15µM IPTG	width(nm)	966.1	80.25	503
B	bMD631	30mM xyl 20µM IPTG	width(nm)	902	106.4	262
C	bMD557	30mM xyl, 40µM IPTG	width(nm)	987.1	87.58	230
C	bMD557	30mM xyl 100µM IPTG	width(nm)	856.5	121.3	266
D	bMD620	0.1m M xyl 0 IPTG	Surface growth	0.755	0.1681	183
D	bMD620	0.5mM xyl 1µM IPTG	Surface growth	1.025	0.171	63
D	bMD620	2.5mM xyl 10µM IPTG	Surface growth	1.146	0.1108	57
D	bMD620	5mM xyl 25µM IPTG	Surface growth	1.174	0.0692	78
D	bMD620	30mM xyl 100µM IPTG	Surface growth	1.282	0.1895	46
D	bMD622	30mM xyl 1mM IPTG	Surface growth	1.194	0.1063	54
D	bMD620	0.1mM xyl 25µM IPTG	Surface growth	0.816	0.2653	17
D	bMD620	0.5mM xyl 25µM IPTG	Surface growth	1.203	0.138	111
D	bMD620	1mM xyl 25µM IPTG	Surface growth	1.182	0.174	59
D	bMD620	2.5mM xyl 25µM IPTG	Surface growth	1.188	0.1229	121
D	bMD620	5mM xyl 25µM IPTG	Surface growth	1.174	0.0691	78
D	bMD620	30mM xyl 25µM IPTG	Surface growth	1.326	0.1969	50
D	bMD620	5mM xyl 1µM IPTG	Surface growth	1.274	0.182	78
D	bMD620	5mM xyl 10µM IPTG	Surface growth	1.256	0.1302	140
D	bMD620	5mM xyl 25µM IPTG	Surface growth	1.174	0.0692	78
D	bMD620	5mM xyl 50µM IPTG	Surface growth	1.288	0.1677	486
D	bMD620	5mM xyl 100µM IPTG	Surface growth	1.353	0.1076	123
D	bMD599		Surface growth	1.263	0.1487	84
D	bAM268		Surface growth	1.147	0.1432	177
D	bAM288	25µM IPTG	Surface growth	1.107	0.1121	51
D	bMD631	1mM xyl 15µM IPTG	Surface growth	1.398	0.1488	187
D	bMD631	30mM xyl 15µM IPTG	Surface growth	1.327	0.0789	49
D	bMD631	30mM xyl 40µM IPTG	Surface growth	1.173	0.1377	47
D	Py79		Surface growth	1.223	0.1527	84
D	bMD620	0.1mM xyl 0 IPTG	Bulk growth	1.49	0.1	5
D	bMD620	0.5mM xyl 1µM IPTG	Bulk growth	1.76	0.09	10
D	bMD620	2.5mM xyl 10µM IPTG	Bulk growth	1.85	0.17	9
D	bMD620	5mM xyl 25µM IPTG	Bulk growth	1.85	0.07	5
D	bMD620	30mM xyl 100µM IPTG	Bulk growth	1.89	0.05	5
D	bMD622	30mM xyl 1mM IPTG	Bulk growth	2	0.03	5
D	bMD620	0.1mM xyl 25µM IPTG	Bulk growth	1.277	0.07	5
D	bMD620	0.5mM xyl 25µM IPTG	Bulk growth	1.98	0.05	5
D	bMD620	1mM xyl 25µM IPTG	Bulk growth	1.88	0.04	5
D	bMD620	2.5mM xyl 25µM IPTG	Bulk growth	1.85	0.03	5
D	bMD620	5mM xyl 25µM IPTG	Bulk growth	2.05	0.13	10
D	bMD620	30mM xyl 25µM IPTG	Bulk growth	1.97	0.03	5
D	bMD620	5mM xyl 1µM IPTG	Bulk growth	1.84	0.18	10
D	bMD620	5mM xyl 10µM IPTG	Bulk growth	1.96	0.14	9
D	bMD620	5mM xyl 25µM IPTG	Bulk growth	1.76	0.05	5
D	bMD620	5mM xyl 50µM IPTG	Bulk growth	1.83	0.03	5
D	bMD620	5mM xyl 100µM IPTG	Bulk growth	1.86	0.05	5
D	bMD599		Bulk growth	1.19	0.04	10
D	bAM268		Bulk growth	1.17	0.03	5
D	bAM288	25µM IPTG	Bulk growth	1.7	0.02	5
D	Py79	25µM IPTG	Bulk growth	2	0.13	26

1207
1208

C - Figure 3

Panel	Strain	Conditions	Width (um)	Width SD	(N)	Filament density	Density SD
B	YS981	0.1mM Xyl	1.3826	0.2	336	0.29	0.28
B	YS981	0.25mM Xyl	1.2808	0.2894	214	0.37	0.35
B	YS981	0.5mM Xyl	1.2557	0.1674	130	0.55	0.42
B	YS981	1mM Xyl	1.0093	0.1128	113	1.49	0.85
B	YS981	1.75mM Xyl	1.0661	0.0969	116	1.36	0.58
B	YS981	2.5mM Xyl	1.0469	0.1315	107	1.64	0.48
B	YS981	5mM Xyl	1.0051	0.0985	92	2.14	0.85
B	YS981	30mM Xyl	1.0124	0.0731	190	2.12	0.83

1209 **D - Figure S3 – Simulation**

Panel	Parameter	Input value	Assay	Filament density	SD	N
A	density	0.7958	Correlated motion	0.8435	0.1207	5
A	density	1.5915	Correlated motion	1.7985	0.1207	5
A	density	2.3873	Correlated motion	2.3873	0.4674	5
A	density	3.1831	Correlated motion	3.3263	0.62	5
A	density	3.9789	Correlated motion	3.7561	0.5261	5
A	density	4.7746	Correlated motion	4.2494	0.795	5
A	density	5.5704	Correlated motion	4.902	0.5997	5
A	density	6.3662	Correlated motion	4.8383	0.6149	5
A	density	7.162	Correlated motion	5.077	0.462	5
A	density	0.7958	Tracking	0.7321	0.2478	5
A	density	1.5915	Tracking	1.4006	0.1332	5
A	density	2.3873	Tracking	1.8462	0.1424	5
A	density	3.1831	Tracking	2.1008	0.2293	5
A	density	3.9789	Tracking	2.7375	0.5559	5
A	density	4.7746	Tracking	2.9444	0.497	5
A	density	5.5704	Tracking	3.0876	0.2999	5
A	density	6.3662	Tracking	3.008	0.3487	5
A	density	7.162	Tracking	3.1831	0.4135	5
B	velocity	20	Correlated motion	2.6101	0.4034	5
B	velocity	25	Correlated motion	3.3263	0.43	5
B	velocity	30	Correlated motion	3.2945	0.5114	5
B	velocity	35	Correlated motion	3.3423	0.2699	5
B	velocity	40	Correlated motion	3.0399	0.1815	5
B	velocity	45	Correlated motion	2.9125	0.2361	5
B	velocity	50	Correlated motion	3.1513	0.3585	5
B	velocity	60	Correlated motion	2.9762	0.2361	5
B	velocity	70	Correlated motion	2.7375	0.215	5
B	velocity	80	Correlated motion	2.5624	0.2414	5
B	velocity	90	Correlated motion	2.9125	0.3716	5
B	velocity	20	Tracking	2.4032	0.2945	5
B	velocity	25	Tracking	2.6261	0.1866	5
B	velocity	30	Tracking	2.451	0.2414	5
B	velocity	35	Tracking	2.4351	0.2293	5
B	velocity	40	Tracking	2.5465	0.4708	5
B	velocity	45	Tracking	2.3237	0.3051	5
B	velocity	50	Tracking	2.6738	0.438	5
B	velocity	60	Tracking	2.642	0.495	5
B	velocity	70	Tracking	3.008	0.3051	5
B	velocity	80	Tracking	2.7056	0.4606	5
B	velocity	90	Tracking	2.2759	0.165	5

Panel	Parameter	Input value	Assay	Filament density	SD	N
C	number	-30	Correlated motion	3.947	0.3009	5
C	number	-25	Correlated motion	3.5173	0.3749	5
C	number	-20	Correlated motion	3.5173	0.4112	5
C	number	-15	Correlated motion	3.3741	0.4271	5
C	number	-10	Correlated motion	3.3104	0.6381	5
C	number	-5	Correlated motion	3.2627	0.5033	5
C	number	0	Correlated motion	3.1831	0.5955	5
C	number	5	Correlated motion	3.4855	0.5912	5
C	number	10	Correlated motion	3.5969	0.1631	5
C	number	15	Correlated motion	3.7083	0.412	5
C	number	20	Correlated motion	3.7879	0.4761	5
C	number	25	Correlated motion	3.581	0.464	5
C	number	30	Tracking	3.6765	0.5261	5
C	angle	-30	Tracking	3.3741	0.3262	5
C	angle	-25	Tracking	2.8648	0.232	5
C	angle	-20	Tracking	3.008	0.3252	5
C	angle	-15	Tracking	2.6897	0.43	5
C	angle	-10	Tracking	2.6579	0.3061	5
C	angle	-5	Tracking	2.451	0.2722	5
C	angle	0	Tracking	2.2918	0.3348	5
C	angle	5	Tracking	2.7215	0.3252	5
C	angle	10	Tracking	2.8966	0.3923	5
C	angle	15	Tracking	2.8011	0.1038	5
C	angle	20	Tracking	2.6897	0.3441	5
C	angle	25	Tracking	2.7693	0.2836	5
C	angle	30	Tracking	3.4218	0.1125	5
D	length	5	Correlated motion	3.0876	0.3348	5
D	length	25	Correlated motion	3.1831	0.1489	5
D	length	50	Correlated motion	3.2786	0.3664	5
D	length	125	Correlated motion	3.1513	0.0907	5
D	length	250	Correlated motion	3.0717	0.5114	5
D	length	300	Correlated motion	3.1354	0.4893	5
D	length	350	Correlated motion	2.5306	0.76	5
D	length	375	Correlated motion	2.5146	0.2293	5
D	length	400	Correlated motion	2.3396	0.1332	5
D	length	450	Correlated motion	2.0531	0.206	5
D	length	500	Correlated motion	1.8303	0.4285	5
D	length	5	Tracking	2.2759	0.1743	5
D	length	25	Tracking	2.3555	0.5415	5
D	length	50	Tracking	2.4351	0.1832	5
D	length	125	Tracking	2.5465	0.1125	5
D	length	250	Tracking	2.5783	0.2615	5
D	length	300	Tracking	2.6579	0.438	5
D	length	350	Tracking	2.5783	0.4344	5
D	length	375	Tracking	2.4669	0.3858	5
D	length	400	Tracking	2.9125	0.3163	5
D	length	450	Tracking	3.0399	0.2945	5
D	length	500	Tracking	2.8011	0.4886	5

1211 **E - Figure 4, S4**

Panel	Strain	Conditions	Parameter	Value	SD	(N)
B, C	YS981	30/0.001	Width	1.3826	0.2	93
B, C	YS981	5/0.025	Width	1.2808	0.2894	214
B, C	YS981	0.5/100	Width	1.2557	0.1674	130
B, E	YS981	30/0.001	Retardance			93
B, E	YS981	5/0.025	Retardance			91
B,E	YS981	0.5/100	Retardance			137
S4A	bMD620	30/0.001	Cell width (TEM)	512.38	45.5616	16
S4A	bMD620	5/0.025	Cell width (TEM)	705.71	51.6678	35
S4A	bMD620	0.5/100	Cell width (TEM)	1138.8	229.043	58
S4A	Py79		Cell width (TEM)	748.08	31.5936	32
S4A	bMD620	30/0.001	Cell wall width (TEM)	14	3.2609	16
S4A	bMD620	5/0.025	Cell wall width (TEM)	15.34	1.6439	35
S4A	bMD620	0.5/100	Cell wall width (TEM)	19.51	3.7475	58
S4A	Py79		Cell wall width (TEM)	15.11	1.3955	32
H, S4B, S4C	bMD620	5/0.025 preshock	Sacculus length	4470	1138	446
H, S4B, S4C	bMD620	5/0.025 preshock	Sacculus Width	782.6	53.03	446
H, S4B, S4C	bMD620	5/0.025 shocked	Sacculus length	3120	973.5	309
H, S4B, S4C	bMD620	5/0.025 shocked	Sacculus Width	676.6	41.38	309
H, S4B, S4C	bMD620	0.5/100 preshock	Sacculus length	4261	1063	145
H, S4B, S4C	bMD620	0.5/100 preshock	Sacculus Width	1283	199.2	145
H, S4B, S4C	bMD620	0.5/100 shocked	Sacculus length	3386	812.6	146
H, S4B, S4C	bMD620	0.5/100 shocked	Sacculus Width	1085	164.9	146
H, S4B, S4C	bMD620	30/0.001 preshock	Sacculus length	3789	1535	1112
H, S4B, S4C	bMD620	30/0.001 preshock	Sacculus Width	586.4	43.09	1112
H, S4B, S4C	bMD620	30/0.001 shocked	Sacculus length	2315	919.6	408
H, S4B, S4C	bMD620	30/0.001 shocked	Sacculus Width	527.6	59.77	408

1212
1213

1214 **F - Figure 5.**

Panel	Strain	Mutation	Conditions	Width (um)	Width SD	(N)	Filament density	Density SD	Source.
A	NO50 - A20S	A20S		0.8671	0.0969	474	1.15	0.39	13
A	NO50 - L322Q	L322Q		0.8387	0.084	661	1.19	0.65	13
A	NO50 - S14A	S14A		0.975	0.1879	559	1.01	0.31	13
A	NO50 - R74C	R74C		0.91	0.1645	517	1.01	0.43	13
A	NO50	WT		1.1343	0.1243	656	1.04	0.24	13
A	NO50 - A53∆	A53∆		1.2579	0.1261	610	0.40	0.23	13
A	NO50 - S185F	S185F		0.9296	0.154	715	0.88	0.37	13
A	NO50 - F84V	F84V		1.2876	0.2494	946	0.39	0.22	13
A	RM478	S14A ∆RodZ		1.3285	0.2075	388	0.33	0.18	14
A	eKC508	WT		1.18	0.11	323	0.41	0.41	15
A	eKC507	E276D		0.97	0.08	220	1.03	0.47	16
A	eKC967	D83E		1.12	0.255	384	0.72	0.17	15
A	eKC968	R124C		1.0061	0.2395	197	0.91	0.26	15
A	eKC969	A174T		1.2832	0.1777	279	0.54	0.27	15
A	eKC407	EC - mrdA		1.1325	0.1199	249	0.83	0.31	16
A	eKC408	ST - mrdA		1.0715	0.1358	131	0.95	0.41	16
A	eKC409	VC - mrdA		1.4799	0.1121	773	0.42	0.16	16
A	eKC410	YP - mrdA		1.1447	0.1887	457	0.85	0.31	16
A	eKC717		0.005% Arab.	1.4657	0.2501	775	0.33	0.13	15
A	eKC717		0.01% Arab.	1.2809	0.1892	561	0.44	0.25	15
A	eKC717		0.05% Arab.	1.229	0.149	794	0.88	0.34	15
A	eKC717		0.1% Arab.	1.2239	0.2842	575	0.88	0.46	15
A	eKC717		0.2% Arab.	1.194	0.2329	239	0.90	0.34	15
B	AV88 pAV20 G5	WT – no repression	100 ng/ml ATc	1.1132	0.1044	812	0.93	0.31	This work.
B	AV88 pAV20 G10		100 ng/ml ATc	1.1284	0.1981	691	0.80	0.37	This work.
B	AV88 pAV20 G14		100 ng/ml ATc	1.6528	0.308	531	0.23	0.21	This work.
B	AV88 pAV20 G20		100 ng/ml ATc	1.9188	0.278	451	0.15	0.09	This work.
B	AV88 pcrRNA G10		100 ng/ml ATc	1.1355	0.1052	1103	0.89	0.44	This work.
B	AV88 pcrRNA G11		100 ng/ml ATc	1.2541	0.1008	878	0.56	0.33	This work.
B	AV88 pcrRNA G14		100 ng/ml ATc	1.2938	0.1323	342	0.56	0.34	This work.
B	AV88 pcrRNA G20		100 ng/ml ATc	1.9238	0.3106	409	0.08	0.07	This work.

1215

38

Table S2 – *B. subtilis* strains used in this study

Strain	Relevant genotype	Source
bMD277	*amyE::Pxyl-mreBCD, minCD (B. megaterium)::erm*	This work
bMD465	*amyE::Pxyl-mreBCD, minCD (B. megaterium)::erm, mreBCD, minC,D::spec (B. megaterium)*	This work
bMK355	*amyE::Pxyl-mreBCD::erm*	This work
bMD543	*amyE::Pxyl-mreBCD::erm ΔmreBCD, ΔminCD::cat*	This work
bMD545	*amyE::Pxyl-mreBCD::erm ΔmreBCD, PmreB-minCD::spec*	This work
bMD599	*ΔponA::kan*	This work
bMK005	*ΔponA::cat*	[17]
bMD554	*yhdG::Phyperspank-ponA::cat*	This work
bMD586	*yhdG::Phyperspank-ponA::cat ΔponA::kan*	This work
bMD594	*yhdG::Pspank-ponA::cat*	This work
bMD598	*yhdG::Pspank-ponA::cat ΔponA::kan*	This work
bMD619	*amyE::Pxyl-mreBCD::erm ΔmreBCD, PmreB-minCD::spec yhdG::Pspank-ponA::cat*	This work
bMD620	*amyE::Pxyl-mreBCD::erm ΔmreBCD, PmreB-minCD::spec yhdG::Pspank-ponA::cat ΔponA::kan*	This work
bMD622	*amyE::Pxyl-mreBCD::erm yhdG::Pspank-ponA::cat ΔponA::kan*	This work
bMD556	*yhdG::Phyperspank-rodA::cat*	This work
bMD580	*yhdG::Phyperspank-rodA::cat ΔrodA::kan*	This work
bMD592	*Pxyl-rodA::erm*	This work
bDR2487	*ΔpbpH::spec*	[18]
bMD627	*Pxyl-rodA::erm ΔpbpH::spec*	This work
bMD563	*yhdG::Phyperspank-pbpA::cat*	This work
bRB776	*yhdG::Pspank-pbpH::phleo ΔpbpH::spec ΔpbpA::erm*	[18]
bMD573	*yhdG::Phyperspank-pbpA::cat ΔpbpH::spec*	This work
bMD574	*yhdG::Phyperspank-pbpA::cat ΔpbpA::erm ΔpbpH::spec*	This work
bMD590	*Pxyl-pbpA::erm*	This work
bMD597	*Pxyl-pbpA::erm ΔpbpH::spec*	This work
bMD557	*amyE::Pxyl-mreBCD::erm yhdG::Phyperspank-rodA::cat*	This work
bMD571	*amyE::Pxyl-mreBCD::erm yhdG::Phyperspank-pbpA::cat*	This work
bRB773	*yhdG::Pspank-pbpA::phleo ΔpbpH::spec ΔpbpA::cat*	[18]
bMD631	*yhdG::Pspank-pbpA::phleo ΔpbpH::spec ΔpbpA::cat Pxyl-rodA::erm*	This work
bYS201	*HaloTag-11aa-pbpA::cat*	This work
bMK385	*amyE::Pxyl-mreBCD::erm ΔmreBCD, PmreB-minCD::spec HaloTag-11aa-pbpA::cat*	This work
bAM268	*ΔpbpF ΔpbpG ΔpbpD ΔponA::kan*	[19]
bAM288	*ΔpbpF ΔpbpG ΔpbpD ΔponA::kan amyE::Phyperspank-rodA-His10::spec*	[19]
bMD88	*Pxyl-mreC::erm*	[12]
bYS09	*mreB-mNeonGreen*	[20]
bYS19	*mreB-SW-msfGFP*	This work
bYS977	*amyE::Pxyl-mreB-SW-msfGFP,mreC,mreD::erm*	This work
bYS979	*amyE::Pxyl-mreB-SW-msfGFP,mreC,mreD::erm, ΔmreBCD, ΔminCD::cat*	This work
bYS981	*amyE::Pxyl-mreB-SW-msfGFP,mreC,mreD::erm, ΔmreBCD, PmreB-minC,D::spec*	This work

Table S3 – *E. coli* strains used in this study

Strain	Relevant genotype	Source
MG1655	Wild-type E. coli	CGSC #6300
NO50	*mreB-msfGFP sw*	[13]
NO50 - A20S	*NO50 with mreB(A20S)*	[13]
NO50 - L322Q	*NO50 with mreB(L322Q)*	[13]
NO50 - ΔA53	*NO50 with mreB(ΔA53)*	[13]
NO50 - S185F	*NO50 with mreB(S185F)*	[13]
NO50 - F84V	*NO50 with mreB(F84V)*	[13]
NO50 - R74C	*NO50 with mreB(R74C)*	[13]
NO50 - S14A	*NO50 with mreB(S14A)*	[14]
RM478	*ΔrodZ, mreB(S14A)-msfGFP*	[14]
KC407	*ΔmrdA csrA::frt, mreB'::msfGFP-mreB'' + pww308 Ec mrdA*	[16]
KC408	*ΔmrdA csrA::frt, mreB'::msfGFP-mreB'' + pww308 St mrdA*	[16]
KC409	*ΔmrdA csrA::frt, mreB'::msfGFP-mreB'' + pww308 Vc mrdA*	[16]
KC410	*ΔmrdA csrA::frt, mreB'::msfGFP-mreB'' + pww308 Yp mrdA*	[16]
NO34	*csrD::kan, mreB::msfGFP-mreB*	[13]
KC507	*csrD::kan, mreB'::msfGFP-mreB'-E276D*	[15]
KC717	*csrD::kan, mreB::msfGFP-mreB,ProdZ◇(frt araC PBAD)*	[15]

KC967	*csrD::kan, mreB'::msfGFP-mreB'-D83E*	15
KC968	*csrD::kan, mreB'::msfGFP-mreB'-R124C*	15
KC969	*csrD::kan, mreB'::msfGFP-mreB'-A174T*	15
AV88	*186:: P_Tet-dCas9, mreB::msfGFP-mreB*	This work
AV88 pAV20 G5	*AV88 with pAV20 G5*	This work
AV88 pAV20 G10	*AV88 with pAV20 G10*	This work
AV88 pAV20 G14	*AV88 with pAV20 G14*	This work
AV88 pAV20 G20	*AV88 with pAV20 G20*	This work
AV88 pcrRNA G10	*AV88 with pcrRNA G10*	This work
AV88 pcrRNA G11	*AV88 with pcrRNA G11*	This work
AV88 pcrRNA G14	*AV88 with pcrRNA G14*	This work
AV88 pcrRNA G20	*AV88 with pcrRNA G20*	This work

1219

Table S4 – Plasmids used in this study

1220

pAV20 G5	*guide RNA is sgRNA pAV20 G5, 5 matching base pairs against GFP*	This work
pAV20 G10	*guide RNA is sgRNA pAV20 G10, 10 matching base pairs against GFP*	This work
pAV20 G14	*guide RNA is sgRNA pAV20 G14, 14 matching base pairs against GFP*	This work
pAV20 G20	*guide RNA is sgRNA pAV20 G20, 20 matching base pairs against GFP*	This work
pcrRNA G10	*guide RNA is native crRNA, 10 matching base pairs against GFP*	This work
pcrRNA G11	*guide RNA is native crRNA, 11 matching base pairs against GFP*	This work
pcrRNA G14	*guide RNA is native crRNA, 14 matching base pairs against GFP*	This work
pcrRNA G20	*guide RNA is native crRNA, 20 matching base pairs against GFP*	This work

1221

1222

Table S5 – Oligonucleotides used in this study

1223

Oligo	Sequence
oJM028	TTCTGCTCCCTCGCTCAG
oJM029	CAGGGAGCACTGGTCAAC
oMD68	TTTTACAGCTGATCCCATAGCGTAG
oMD69	CTGGACAGGGCTCAGGTCCGGGATCTGGCATGAGGAGAAATAAACCAAAAAAGCAAAATC
oMD72	AACATCACCTTTTCTATTTAATCGATCCATTCAAATACAGATGCATTTTATTTC
oMD73	ATACGAACGGTACTGAGCGAGGGAGCAGAAGAATTCGAGCTTGCATGCCTG
oMD75	CAGCCGATAACCTTTTATTTGGCTG
oMD96	TTTCACCAGAAGAAAACGTCCAATG
oMD108	ACGAACGGTAGTTGACCAGTGCTCCCTGTCTTGACACTCCTTATTTGATTTTTTGAAGAC
oMD116	CAGCCAGAACTGCTATCAATATCACTAC
oMD125	TACGAACGGTAGTTGACCAGTGCTCCCTGTTTACAGAAAGAAAAGACACTCAAGTAAGAG
oMD134	CCGAGCAGGGAAGATATTGAAG
oMD191	TTTGGATGGATTCAGCCCGATTG
oMD196	GGGCAAGGCTAGACGGG
oMD197	TCACATACTCGTTTCCAAACGGATC
oMD226	GGTAGTTCCTCCTTAATCGATCCATTCAAATACAGATGCATTTTATTTC
oMD227	TTTGAATGGATCGATTAAGGAGGAACTACCATGTTTGGAATCGGTACTAGAGACC
oMD228	TTTCGGTAAGTCCCGTCTAGCCTTGCCCTTAAGAACGAACACCAAAGAATCGTTTAATAC
oMD232	GGTAGTTCCTCCTTAAAGCTTAATTGTTATCCGCTCACAAT
oMD234	ATACGAACGGTACTGAGCGAGGGAGCAGAATAATGGATTTCCTTACGCGAAATACG
oMD298	ATACGAACGGTAGTTGACCAGTGCTCCCTGATGTATGTATCTTCCTTTCTTAAAGC
oMD299	ATACGAACGGTACTGAGCGAGGGAGCAGAATGTGATAGAATCAAAGAGAAGAATCTGAC
oMD300	CTCTTCCTTTAACGGCCGATTC
oMD308	ATGTATGTATCTTCCTTTCTTAAAGCAAAAATACC
oMD313	ACAGCATATGCTTTGTCAGATTCTTCTCTTTGATTCTATCACATTAAGAACGAACACCAAAGAATCGTTTAATAC
oMD314	AAGAGAAGAATCTGACAAAGCATATGCTGTGTCAGGTTTTTTTTGTTTTTCAGGGAGCACTGGTCAAC
oMD315	ATACGAACGGTACTGAGCGAGGGAGCAGAAGCCTGCTTTGTTCTTGACTAAACC
oMD316	TAACAATTAAGCTTTAAGGAGGAACTACCATGAGGAGAAATAAACCAAAAAAGCAAAATC
oMD328	CCTGTTTCAGGTTCGGTGTATAC
oMD329	ATACGAACGGTAGTTGACCAGTGCTCCCTGTAAACGTCACTTCCTTTCCAGC
oMD334	TTTGAATGGATCGATTAAGGAGGAACTACCATGTTTGGAATTGGTGCTAGAGAC
oMD364	ATAACAATTAAGCTTTAAGGAGGAACTACCATGAGTCGATATAAGAACAGCAAAGC
oMD365	ATAACAATTAAGCTTTAAGGAGGAACTACCATGTCAGATCAATTTAACAGCCGTG
oMD367	ACGAACGGTAGTTGACCAGTGCTCCCTGGCCAAGAACAGAAAAGAGGCGGCCTGTATGGC

40

oMD369	GAAAAGAGGCGGCCTGTATGGCCGTCAAGAATTAAAAAGATAACTTCTGTATTTCGTCAG
oMD370	GAAAAGAGGCGGCCTGTATGGCCGTTAATTTGTTTTTTTCAATGGATGATGAGTTTGTTTG
oMD371	CGGCCATACAGGCCG
oMD372	GCTGACGGTAAAATCGGCAATATC
oMD379	TGTTACATATTGCTGCTTTTTGGTCTTCACATGTATGTATCTTCCTTTCTTAAAGC
oMD380	GTGAAGACCAAAAAGCAGCAATATG
oMD381	ATACGAACGGTACTGAGCGAGGGAGCAGAAAAAAACAAAAAAAACCTGACACAGCATATG
oMD382	ATACGAACGGTAGTTGACCAGTGCTCCCTGTGTGATAGAATCAAAGAGAAGAATCTGAC
oMD386	GTTTTCGCTGCTATATGACTGATTAGC
oMD387	ATACGAACGGTACTGAGCGAGGGAGCAGAATATGCAGACAGCCTTTACAGAGG
oMD388	ATACGAACGGTAGTTGACCAGTGCTCCCTGTCTATCCCGCCTTACATTTTCATCG
oMD389	TGTTGTATGGATTTTCATCTTTACAGGTG
oMD393	ATGGATCGATTAAATAGAAAAGGTGATGTTATGAGGAGAAATAAAC
oMD394	TTTGAATGGATCGATTAAGGAGGAACTACCATGAGTCGATATAAGAAACAGCAAAGC
oMD395	TGCACAAAAAAAGACAGCCTCTG
oMK001	GCCTTATCCTTTCCTCCGCC
oMK002	CTGAGCGAGGGAGCAGAACATCTCAACCTTTCGTTAATCAACC
oMK005	TACGAACGGTAGTTGACCAGTGCTCCCTGGTACACAATAAAAAACCTCCCGTTTTAACAG
oMK006	CGTGTACAAGCAAAGCAGAATGAAC
oMK221	TTCTTTCGGTAAGTCCCGTCTAGCCTTGCCCTTACTCATCTCTCAATTCTTTCTTTAGAC
oYS34	TTCTTCCCCTTTTCGCATACTTGAGCCGCTGATTTCCATTTTAATCGCTTCAGCCG
oYS35	GCGATTAAAATGGAAATCAGCGGCTCAAGTATGCGAAAAGGGGAAGAATTGTTTAC
oYS36	AGCTTCTGCAGATCCGCCAGGTGCTCCAGATTTGTAAAGTTCATCCATTCCATGC
oYS37	GATGAACTTTACAAATCTGGAGCACCTGGCGGATCTGCAGAAGCTCCTGAA
oYS598	GCCAGATCCCGGACCTGAGCCCTGTCCAGAGCCGCCGCTGATTTCTAAGGTAGAAAG
oYS599	GAGTGTCTTTTCTTTCTGTAAATAGAAAAGGTGATGTTATGGCAGAAATCGGTACTGGC
V162	GGTGCTTTTTTTGAACGAAAACTCACGTTAAGGGATTTTG
V163	TAGCTGTCAACACTGAGCGTCAGACCCC
V164	ACGCTCAGTGTTGACAGCTAGCTCAGTCCTAGGTATAATACTAG
V165	CGAGACCTAGACTGGTCTCACTAGTATTATACCTAGGACTGAGCTAGCTG
V166	ACTAGTGAGACCAGTCTAGGTCTCGTTTAGAGCTAGAAATAGCAAGTTAAAATAAGG
V167	GAGTTTTCGTTCAAAAAAAAGCACCGACTCGGT
V272	ctagtCACCACGAACAGAGAATTTGgt
V273	ctagtGTGGTGGAACAGAGAATTTGgt
V274	ctagtGTGGTGCTTGAGAGAATTTGgt
V275	ctagtGTGGTGCTTGTCTCTATTTGgt
V279	tagtAGACCCACGGAAGTAACGGA
V280	taaaacCAAATTCTCTGTTCGTGGTGa
V281	taaaacCAAATTCTCTGTTCCACCACa
V282	taaaacCAAATTCTCTCAAGCACCACa
V283	taaaacCAAATAGAGACAAGCACCACa
V287	aaacTCCGTTACTTCCGTGGGTCT

1224

1225

1226

Supplemental References

1. Grimm, J. B. *et al.* A general method to improve fluorophores for live-cell and single-molecule microscopy. *Nat Meth* **12,** 244–250 (2015).

2. Ursell, T. *et al.* Rapid, precise quantification of bacterial cellular dimensions across a genomic-scale knockout library. *BMC Biology* **15,** 17 (2017).

3. Vadia, S. & Levin, P. A. Growth rate and cell size: a re-examination of the growth law. *Curr Opin Microbiol* **24,** 96–103 (2015).

4. Ursell, T. S. *et al.* Rod-like bacterial shape is maintained by feedback between cell curvature and cytoskeletal localization. *Proc Natl Acad Sci USA* **111,** E1025–34 (2014).

5. Wiseman, P. W. Image correlation spectroscopy: mapping correlations in space, time, and reciprocal space. - PubMed - NCBI. *Fluorescence Fluctuation Spectroscopy (FFS), Part A* **518,** 245–267 (2013).

6. Sharpe, M. E., Hauser, P. M., Sharpe, R. G. & Errington, J. Bacillus subtilis cell cycle as studied by fluorescence microscopy: constancy of cell length at initiation of DNA replication and evidence for active nucleoid partitioning. *J Bacteriol* **180,** 547–555 (1998).

7. Vollmer, W., Blanot, D. & de Pedro, M. A. Peptidoglycan structure and architecture. *FEMS Microbiol Rev* **32,** 149–167 (2008).

8. Kner, P., Chhun, B. B., Griffis, E. R., Winoto, L. & Gustafsson, M. G. L. Super-resolution video microscopy of live cells by structured illumination. *Nat Meth* **6,** 339–342 (2009).

9. Vigouroux, A., Oldewurtel, E., Cui, L., Bikard, D. & van Teeffelen, S. Tuning dCas9's ability to block transcription enables robust, noiseless knockdown of bacterial genes. *Molecular Systems Biology* **14,** e7899 (2018).

10. Kall, L., Storey, J. D. & Noble, W. S. Non-parametric estimation of posterior error probabilities associated with peptides identified by tandem mass spectrometry. *Bioinformatics* **24,** i42–i48 (2008).

11. Gibson, D. G. *et al.* Enzymatic assembly of DNA molecules up to several hundred kilobases. *Nat Meth* **6,** 343–U41 (2009).

12. Schirner, K. *et al.* Lipid-linked cell wall precursors regulate membrane association of bacterial actin MreB. *Nat. Chem. Biol.* **11,** 38–45 (2015).

13. Ouzounov, N. *et al.* MreB Orientation Correlates with Cell Diameter in Escherichia coli. *Biophys J* **111,** 1035–1043 (2016).

14. Morgenstein, R. M. *et al.* RodZ links MreB to cell wall synthesis to mediate MreB rotation and robust morphogenesis. *Proc Natl Acad Sci USA* **112,** 12510–12515 (2015).

15. Colavin, A., Shi, H. & Huang, K. C. RodZ modulates geometric localization of the bacterial actin MreB to regulate cell shape. *Nat Comms* **9,** 1280 (2018).

16. Tropini, C. *et al.* Principles of Bacterial Cell-Size Determination Revealed by Cell-Wall Synthesis Perturbations. *Cell Reports* **9,** 1520–1527 (2014).

17. Cho, H. *et al.* Bacterial cell wall biogenesis is mediated by SEDS and PBP polymerase families functioning semi-autonomously. *Nat Microbiol* **1,** 16172 (2016).

18. Garner, E. C. *et al.* Coupled, circumferential motions of the cell wall synthesis machinery and MreB filaments in B. subtilis. *Science* **333,** 222–225 (2011).

19. Meeske, A. J. *et al.* SEDS proteins are a widespread family of bacterial cell wall polymerases. *Nature* **537,** 634–638 (2016).

20. Hussain, S. *et al.* MreB filaments align along greatest principal membrane curvature to orient cell wall synthesis. *Elife* **7,** 1239 (2018).